Use of WRF-Hydro to Simulate Runoff-Generated Debris Flow Hazards in Burn Scars

Chuxuan Li[1,1], Alexander L Handwerger[2,2], Jiali Wang[3,3], Wei Yu[4,4], Xiang Li[1,1], Noah Joseph Finnegan[5,5], Yingying Xie[6,6], Giuseppe Buscarnera[1,1], and Daniel E Horton[1,1]

[1]Northwestern University
[2]Jet Propulsion Laboratory, Caltech
[3]Argonne National Laboratory (DOE)
[4]Weather Tech LLC.
[5]University of California, Santa Cruz
[6]Purdue University

November 30, 2022

Abstract

In steep wildfire-burned terrains, intense rainfall can produce large volumes of runoff that can trigger highly destructive debris flows. The ability to accurately characterize and forecast debris-flow hazards in burned terrains, however, remains limited. Here, we augment the Weather Research and Forecasting Hydrological modeling system (WRF-Hydro) to simulate both overland and channelized flows and assess postfire debris-flow hazards over a regional domain. We perform hindcast simulations using high-resolution weather radar-derived precipitation and reanalysis data to drive non-burned baseline and burn scar sensitivity experiments. Our simulations focus on January 2021 when an atmospheric river triggered numerous debris flows within a wildfire burn scar in Big Sur – one of which destroyed California's famous Highway 1. Compared to the baseline, our burn scar simulation yields dramatic increases in total and peak discharge, and shorter lags between rainfall onset and peak discharge. At Rat Creek, where Highway 1 was destroyed, discharge volume increases eight-fold and peak discharge triples relative to the baseline. For all catchments within the burn scar, we find that the median catchment-area normalized discharge volume increases nine-fold after incorporating burn scar characteristics, while the 95th percentile volume increases 13-fold. Catchments with anomalously high hazard levels correspond well with post-event debris flow observations. Our results demonstrate that WRF-Hydro provides a compelling new physics-based tool to investigate and potentially forecast postfire hydrologic hazards at regional scales.

Augmentation and Use of WRF-Hydro to Simulate Overland Flow- and Streamflow-Generated Debris Flow Hazards in Burn Scars

Chuxuan Li[1], Alexander L. Handwerger[2,3], Jiali Wang[4], Wei Yu[5,6], Xiang Li[7], Noah J. Finnegan[8], Yingying Xie[9,10], Giuseppe Buscarnera[7], and Daniel E. Horton[1]

[1] Department of Earth and Planetary Sciences, Northwestern University, Evanston, IL, 60208, USA

[2] Joint Institute for Regional Earth System Science and Engineering, University of California, Los Angeles, CA, 90095, USA

[3] Jet Propulsion Laboratory, California Institute of Technology, Pasadena, CA, 91109, USA

[4] Environmental Science Division, Argonne National Laboratory, Lemont, IL, 60439, USA

[5] Cooperative Institute for Research in Environmental Sciences, University of Colorado Boulder, CO, 80309, USA

[6] NOAA/Global Systems Laboratory, 325 Broadway Boulder, Denver, CO, 80305-3328, USA

[7] Department of Civil and Environmental Engineering, Northwestern University, Evanston, IL, 60208, USA

[8] University of California Santa Cruz, Department of Earth and Planetary Sciences, Santa Cruz, CA, 95064, USA

[9] Program in Environmental Sciences, Northwestern University, 2145 Sheridan Road, Evanston, IL, 60208, USA

[10] Department of Biological Sciences, Purdue University, 915 W State St, West Lafayette, IN 47907, USA

Correspondence to: Chuxuan Li (chuxuanli2020@u.northwestern.edu)

Abstract

In steep wildfire-burned terrains, intense rainfall can produce large volumes of runoff that can trigger highly destructive debris flows. The ability to accurately characterize and forecast debris-flow hazards in burned terrains, however, remains limited. Here, we augment the Weather Research and Forecasting Hydrological modeling system (WRF-Hydro) to simulate both overland and channelized flows and assess postfire debris-flow hazards over a regional domain. We perform hindcast simulations using high-resolution weather radar-derived precipitation and reanalysis data to drive non-burned baseline and burn scar sensitivity experiments. Our simulations focus on January 2021 when an atmospheric river triggered numerous debris flows within a wildfire burn scar in Big Sur – one of which destroyed California's famous Highway 1. Compared to the baseline, our burn scar simulation yields dramatic increases in total and peak discharge, and shorter lags between rainfall onset and peak discharge. At Rat Creek, where Highway 1 was destroyed, discharge volume increases eight-fold and peak discharge triples relative to the baseline. For all catchments within the burn scar, we find that the median catchment-area normalized discharge volume increases nine-fold after incorporating burn scar characteristics, while the 95th percentile volume increases 13-fold. Catchments with anomalously high hazard levels correspond well with post-event debris flow observations. Our results demonstrate that WRF-Hydro provides a compelling new physics-based tool to investigate and potentially forecast postfire hydrologic hazards at regional scales.

Short Summary

In January 2021 a storm triggered numerous debris flows in a wildfire burn scar in California. We use a hydrologic model to assess debris flow hazards in pre-fire and postfire scenarios. Compared to pre-fire conditions, the postfire simulation yields dramatic increases in total and peak discharge, substantially increasing debris flow hazards. Our work demonstrates the utility of 3-D hydrologic models for investigating and potentially forecasting postfire debris flow hazards at regional scales.

1 Introduction

Following intense rainfall, areas with wildfire burn scars are more prone to flash flooding (Neary et al., 2003; Bart & Hope 2010; Bart 2016) and runoff-generated debris flow hazards than unburned areas (Moody et al., 2013; Ice et al., 2004; Shakesby & Doerr, 2006). After wildfire, reduced tree canopy interception, decreased soil infiltration due to soil-sealing effects (Larsen et al., 2009), and increased soil water repellency – especially in hyper-arid environments (Dekker and Ritsema, 1994; Doerr and Thomas, 2000; MacDonald and Huffman, 2004) – increases excess surface water, and on sloped terrains leads to overland flow (Shakesby & Doerr, 2006; Stoof et al., 2012). As water moves down hillslopes and erosion adds sediment to water-dominated flows, clear water floods can transition to turbulent and potentially destructive debris flows (Meyer & Wells, 1997; Cannon et al., 2001, 2003; Santi et al., 2008). In contrast to debris flows initiated by shallow landslides, this rainfall-runoff process has been identified as the major cause for postfire debris flows in the western U.S. (Cannon, 2001; Cannon et al., 2003, 2008; Kean et al., 2011; Nyman et al., 2015; Parise & Cannon, 2012), and in other regions with Mediterranean climates (Mitsopoulos & Mironidis, 2006; Bisson et al., 2005; Parise & Cannon, 2008, 2009; Rosso et al., 2007). In California, because climate change is projected to increase the intensity and frequency of wet-season precipitation (Swain et al., 2018; Polade et al., 2017), increase wildfire potential (Swain, 2021; Brown et al., 2021), and extend the wildfire season (Goss et al., 2020), occurrence and intensity of postfire debris flows are likely to increase (Cannon et al., 2009; Kean & Staley, 2021; Oakley, 2021).

To assess postfire debris flow hazards, statistical approaches including empirical models and machine-learning techniques are commonly used in both research and operational settings (Gardner et al., 2014; Cannon et al., 2010; Staley et al., 2016; Cui et al., 2019; Nikolopoulos et al., 2018; Friedel 2011a, 2011b). Statistical approaches are useful for identifying and characterizing relationships amongst contributing environmental factors and are helpful in operational settings due to low computational costs and the potential for rapid assessment. For example, the U.S. Geological Survey (USGS) currently employs a statistical approach in their Emergency Assessment of Postfire Debris-flow Hazards that consists of a logistic regression model to predict the likelihood of post-wildfire debris flows (e.g., Staley et al., 2016; Cannon et al., 2010), and a multiple linear regression model to predict debris flow volumes (Gartner et al., 2014). Machine-learning techniques have also been used to predict postfire debris flows in the western U.S. (Nikolopoulos et al., 2018; Friedel 2011a, 2011b). For example, self-organizing maps and genetic programming were used to predict postfire debris flow occurrence (Friedel 2011b) and volumes (Friedel 2011a), respectively. Compared to the current USGS predictive models, genetic programming was posited to be more useful in solving non-linear multivariate problems (Friedel 2011a), while a random forest algorithm demonstrated increased performance in predicting postfire debris flow occurrence (Nikolopoulos et al., 2018). Despite the utility and advantages of data-driven hazard prediction approaches, these techniques do not simulate the underlying physics, which limits their utility in developing a better process-based understanding of debris flow mechanics, limits their applicability in climatological and geographic settings different than their training sites, and limits their use in non-stationary conditions (e.g., under changing climatic conditions).

In contrast, physics-based models that simulate spatially-explicit hydrologic and mass wastage processes are well-suited for mechanistic sensitivity analyses in diverse settings, but applications of these models have tended to focus on landslide-induced debris flows (e.g., Iverson & George, 2014; George & Iverson, 2014), rather than runoff-generated debris flows which are more common in postfire areas (Cannon et al., 2001, 2003; Santi et al., 2008). Studies that have investigated postfire hydrologic responses using process-based models have largely focused on short-term responses in individual catchments at high spatiotemporal resolutions (McGuire et al., 2016, 2017; Rengers et al., 2016) or long-term runoff responses at coarse temporal resolutions (Rulli & Rosso, 2007; McMichael & Hope, 2007). For example, process-based models have employed shallow water equations to understand the triggering and transport mechanisms of postfire debris flows in single catchments (McGuire et al., 2016, 2017) and to investigate the timing of postfire debris flows in three separate catchments (Rengers et al., 2016), the latter of which also assessed the efficacy of a simplified kinematic wave approach. In addition to individual catchment applications, process-based models often adopt simplifications that can limit effective prediction and hypothesis testing to overcome computational limits. For example, the kinematic runoff and erosion model (KINEROS2) simplifies drainage basins into 1-dimensional channels and hillslope patches (Canfield & Goodrich, 2005; Goodrich et al., 2012; Sidman et al., 2015), and the Hydrologic Modeling System (HEC-HMS) uses an empirically-based curve number method to estimate saturation excess water (Cydzik et al., 2009), which cannot resolve infiltration excess overland flow, a critical process in burn scars (Chen et al., 2013).

Given the current state of debris flow hazard assessment and prediction in previously burned terrains, in addition to the growing influence of anthropogenic climate change on wildfire and extreme precipitation, development of physics-based hazard assessment tools that can be used in both hindcast investigations and forecasting applications is needed. Furthermore, due to the diverse morphology of precipitation events and their interaction with geographically distributed wildfire burn scars, development of tools that can assess hazards over regional domains, particularly in operational forecasting applications, is critical. Here to advance the field of burn scar debris flow hazard assessment, we explore the use of the physics-based and fully-distributed Weather Research and Forecasting Hydrological modeling system version 5.1.1 (WRF-Hydro). WRF-Hydro is an open-source community model developed by the National Center for Atmospheric Research (NCAR). It is the core of National Oceanic and Atmospheric Administration's (NOAA) National Water Model forecasting system, and has been used extensively to study channelized flows (e.g., Lahmers et al., 2020; Wang et al., 2019). Here, we modify WRF-Hydro to output high temporal resolution fine-scale (100 m) debris flow-relevant overland flow; a process computed using a fully unsteady, explicit, finite difference diffusive wave formulation. Previous efforts, employing shallow water equations, diffusive, kinematic, and diffusive-kinematic wave models, have demonstrated that water-only models can provide critical insights on runoff-driven debris flow behavior (Arattano & Savage, 1994; McGuire & Youberg, 2020; Arratano & Franzi, 2010; Di Cristo et al., 2021), even in burned watersheds (Rengers et al., 2016).

To test and demonstrate the utility of WRF-Hydro in debris flow studies, we investigate the January 2021 debris flow events within the Dolan burn scar on the Big Sur coast of central California (Fig. 1a–b). We first identify multiple debris flow sites using optical and radar remote sensing data and field investigations. We then calibrate WRF-Hydro against ground-based soil moisture and streamflow observations and use it to study the effects of burn scars on debris flow hydrology and changes in hazard potential. The paper is organized as follows. Section 2 describes our debris flow identification approach and historical context. Section 3 presents a description of

WRF-Hydro. Section 4 describes the simulation, calibration, and validation of WRF-Hydro. Section 5 presents the results. Section 6 discusses the results and Sect. 7 provides a conclusion.

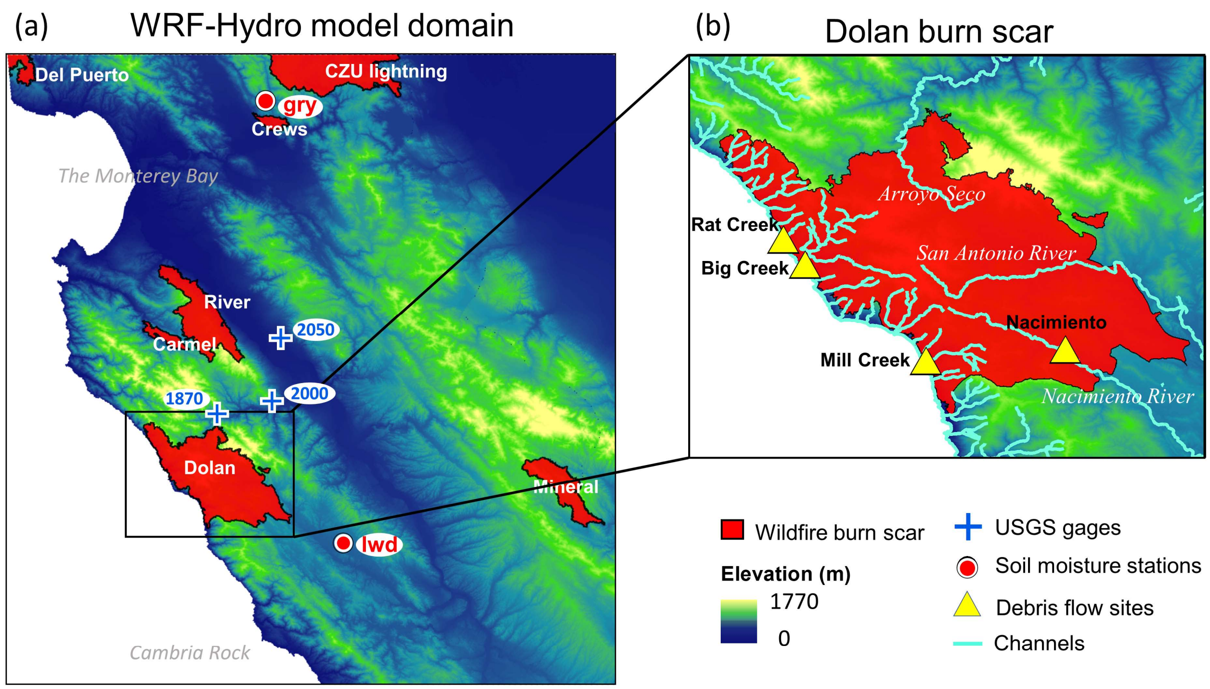

Fig. 1| WRF-Hydro model domain and Dolan burn scar. (a) WRF-Hydro model domain depicting topography, 2020 wildfire season burn scars, and PSL soil moisture and USGS stream gage observing sites. The black rectangle outlines (b) the Dolan burn scar inset, in which debris flow locations and major streams are marked and labeled.

2 Study domain and debris flow identification methodology

The Dolan wildfire burned from August 18th till December 31st, 2020. 55% of areas within the fire perimeter were burned at moderate-to-high severity (Burned Area Emergency Response, 2020). After the fire, USGS Emergency Assessment of Postfire Debris-flow Hazards produced a debris flow hazard assessment using a design storm based statistical model (USGS, 2020). On January 27–29, 2021, an atmospheric river (AR) made landfall on the Big Sur coast, bringing more than 300 mm of rainfall to California's Coast Ranges (Fig. 2), with a peak rainfall rate of 24 mm h^{-1}. During the AR event, a section of California State Highway 1 (CA1) at Rat Creek was destroyed by a debris flow. CA1 was subsequently closed for three months and rebuilt at a cost of ~$11.5M (Los Angeles Times, 2021).

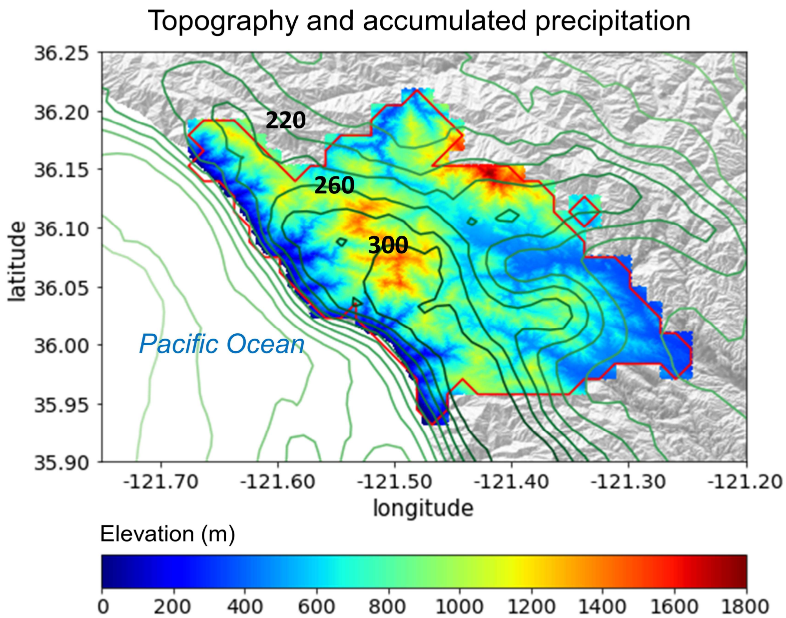

Fig. 2| The topography (shading; m) and MRMS accumulated precipitation (contour lines; mm) during the AR event from January 27th 00:00 to 29th 23:00 in the Dolan burn scar. Contour line interval for accumulated precipitation is 20 mm, and lines of 220, 260, and 300 mm are labeled. The red polygon outlines the perimeter of the Dolan burn scar.

2.1 Debris flow identification from remote sensing and field work

In addition to the Rat Creek debris flow, which made national news (Los Angeles Times, 2021), we identified three other debris flows using a combination of field investigation, and open access satellite optical and synthetic aperture radar (SAR) images (Fig. 3 and Fig. B1). We examined relative differences in normalized difference vegetation index (rdNDVI) defined by (Scheip & Wegmann, 2021):

$$rdNDVI = \frac{NDVI_{post} - NDVI_{pre}}{\sqrt{NDVI_{pre} + NDVI_{post}}} \times 100 \quad (1)$$

where $NDVI_{pre}$ and $NDVI_{post}$ are the pre- and post-event normalized difference vegetation index (NDVI) images computed following:

$$NDVI = \frac{NIR - R}{NIR + Red} \quad (2)$$

where *NIR* is the near-infrared response and *Red* is the visible red response. rdNDVI was calculated from Sentinel-2 satellite data using the HazMapper v1.0 Google Earth Engine application (Scheip & Wegmann, 2021). HazMapper requires selection of an event date, pre-event window (months), post-event window (months), max cloud cover (%) and slope threshold (°). These input requirements filter the number of images used to calculate the rdNDVI. We set the event date to 27 January 2021 and used a 3 month pre- and post-event window with 0% max cloud cover and a 0° slope threshold to identify vegetation loss associated with the debris flows. We then created a binary map to highlight debris flows (and other vegetation loss) pixels above a rdNDVI vegetation loss threshold. We removed all pixels with rdNDVI > -10.

Lastly, we searched for debris flows (and other ground surface deformation) by examining SAR backscatter change with data acquired by the Copernicus Sentinel-1 (S1) satellites (see full description in Handwerger et al., in review). We measured the change in SAR backscatter by using the log ratio approach, defined as

$$I_{ratio} = 10 \times log_{10}(\frac{{\sigma_{pre}}^0}{{\sigma_{post}}^0}) \quad (3)$$

where σ_{pre}^0 is a pre-event image stack (defined as the temporal median) of SAR backscatter and σ_{post}^0 is a post-event image stack. Similar to the HazMapper method, our approach requires selection of an event date, pre-event window (months), post-event window (months) and slope threshold (°). No cloud-cover threshold is needed since SAR penetrates clouds. We used a 3 month pre- and post-event window and 0° slope threshold to identify ground surface changes associated with the debris flows. We then created a binary map to highlight debris flows by removing all pixels with I_{ratio} < 99th percentile value.

Identified debris flow source areas and deposition sites were confirmed by field investigation (N.J. Finnegan) and named after the locations where they deposited (i.e., Big Creek, Mill Creek, and Nacimiento). We note that there were likely more debris flows triggered during the AR event. However, given the primary goal of this study – to demonstrate the utility of WRF-Hydro – a comprehensive cataloging of debris flows is beyond this study's scope.

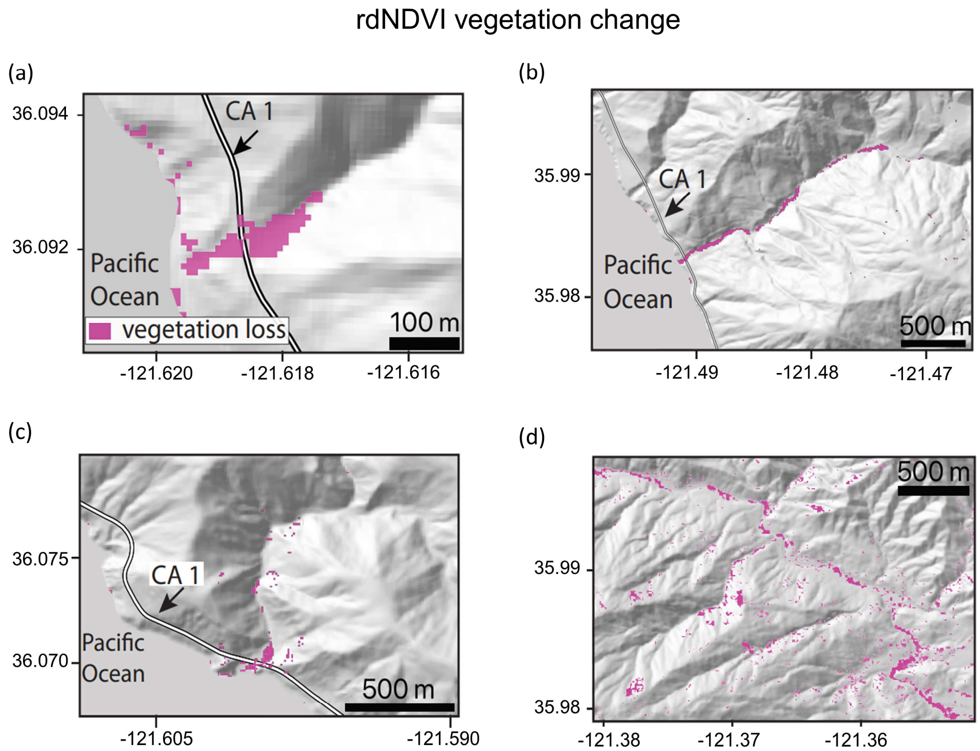

Fig. 3| Identified debris flow sites using rdNDVI vegetation change within the Dolan burn scar. We convert the rdNDVI data into a binary map by setting a threshold value, which yield only the likely debris flow locations. (a)–(d) Sentinel-2 rdNDVI vegetation change at (a) Rat Creek, (b) Mill Creek, (c) Big Creek, and (d) the Nacimiento River.

3 WRF-Hydro

3.1 Model description

WRF-Hydro is an open-source physics-based community model that simulates land surface hydrologic processes. It includes the Noah-Multiparameterization (Noah-MP) land surface model (LSM; Niu et al., 2011), terrain routing module, channel routing module, and a conceptual baseflow bucket model. The Noah-MP LSM is a 1-dimensional column model that calculates vertical energy fluxes (i.e., sensible and latent heat, net radiation), moisture (i.e., canopy interception, infiltration, infiltration excess, deep percolation), and soil thermal and moisture states on the LSM grid (1 km in our application). The infiltration excess, ponded water depth, and soil moisture are then disaggregated using a time-step weighted method (Gochis & Chen, 2003) and sent to the terrain routing module which simulates subsurface and overland flows on a finer terrain routing grid (100 m in our application). According to the mass balance, local infiltration excess, overland flow, and exfiltration from baseflow contribute to the surface head which flows into river channels if defined retention depth is exceeded. The channel routing module then calculates channelized flows assuming a trapezoidal channel shape (Fig. B2). Parameters related to the trapezoidal channel, such as channel bottom width (B_w), Manning's roughness coefficient (n), and channel side slope (z) are functions of channel stream order (Fig. B3 and Table B1). Computed streamflow is then output on the 100 m grid. Equations used to compute infiltration excess, overland flow, and channelized flow are provided in Sect. 3.3 and 3.4.

By default, WRF-Hydro uses Moderate Resolution Imaging Spectroradiometer (MODIS) Modified International Geosphere-Biosphere Program (IGBP) 20-category land cover product as land cover (Fig. B4) and 1-km Natural Resources Conservation Service State Soil Geographic (STATSGO) database for soil type classification (Fig. B5; Miller & White, 1998). Land surface properties including canopy height (HVT), maximum carboxylation rate (VCMX25), and overland flow roughness (OV_ROUGH2D) are functions of land cover type (Table B2 & Fig. B4). Default soil hydraulic parameters in WRF-Hydro (i.e., soil porosity, grain size distribution index, and saturated hydraulic conductivity) are based on Cosby et al.'s (1984) soil analysis (Table B3) and are used to map onto the STATSGO 16 soil texture types (Fig. B5).

3.2 Meteorological forcing files

WRF-Hydro is used in standalone mode (i.e., it is not interactively coupled with the atmospheric component of WRF), but rather is forced with a combination of Phase 2 North American Land Data Assimilation System (NLDAS-2) meteorological data and Multi-Radar/Multi-Sensor System (MRMS) radar-only quantitative precipitation (Zhang et al., 2011, 2014, 2016). A description of the MRMS dataset and uncertainties therein can be found in Appendix A. NLDAS-2 provides hourly forcing data including incoming shortwave and longwave radiation, 2-m specific humidity and air temperature, surface pressure, and 10-m wind speed at 1/8-degree spatial resolution. MRMS provides hourly precipitation rate at 1-km resolution.

3.3 Overland flow routing and output

The Noah-MP LSM calculates rate of infiltration excess following Chen & Dudhia (2001):

$$\frac{\partial h}{\partial t} = \frac{\partial P_d}{\partial t}\left\{1 - \frac{\left[\sum_{i=1}^{4} \Delta D_i(\theta_s - \theta_i)\right]\left[1 - exp\,(-k\frac{K_s}{K_{ref}}\,\delta_t)\right]}{P_d + \left[\sum_{i=1}^{4} \Delta D_i(\theta_s - \theta_i)\right]\left[1 - exp\,(-k\frac{K_s}{K_{ref}}\,\delta_t)\right]}\right\} \tag{4}$$

where *h* (m) is the surface water depth and *t* is the time. P_d (m) is the precipitation not intercepted by the canopy; ΔD_i (m) is the depth of soil layer i; θ_i is the soil moisture in soil layer i; θ_s is the soil porosity; K_s (m s^{-1}) is the saturated hydraulic conductivity; K_{ref} is 2×10^{-6} m s^{-1} which represents the saturated hydraulic conductivity of the silty–clay–loam soil texture chosen as a reference; δ_t (s) is the model time step; and k which is equal to 3.0 is the runoff–infiltration partitioning parameter [the same as kdt_{ref} in Chen & Dudhia (2001)].

Noah-MP passes excess water to the terrain routing module, which simulates overland flow using a 2-dimensional fully-unsteady, explicit, finite-difference diffusive wave equation adapted from Julien et al. (1995) and Ogden (1997). It is considered superior to the traditionally used kinematic wave formulation in that it accounts for backwater effects and flow over adverse slopes. The diffusive wave formulation is the simplified form of the Saint Venant equations, i.e., continuity and momentum equations for a shallow water wave. The 2-dimensional continuity equation for a flood wave is:

$$\frac{\partial h}{\partial t} + \frac{\partial q_x}{\partial x} + \frac{\partial q_y}{\partial y} = i_e \tag{5}$$

where h is the surface flow depth, q_x and q_y are the unit discharges in the x- and y-directions, respectively, and i_e is the infiltration excess. Manning's equation which considers momentum loss is used to calculate q. In the x-direction:

$$q_x = \alpha_x h^{\beta} \tag{6}$$

Where β is a unit dependent coefficient equal to $\frac{5}{3}$, and

$$\alpha_x = \frac{S_{fx}^{1/2}}{n_{ov}} \tag{7}$$

where n_{ov} is the tunable overland flow roughness coefficient. The momentum equation in the x-direction is given by:

$$S_{fx} = S_{ox} - \frac{\partial h}{\partial x} \tag{8}$$

where S_{fx} is the friction slope, $S_{ox}$is the terrain slope, and $\frac{\partial h}{\partial x}$ is the change in surface flow depth in the x-direction.

Off-the-shelf, WRF-Hydro does not output overland flow at terrain routing grids (100 m), however it is computed in the background to determine channelized streamflow. One key advance made in this work is that we modified WRF-Hydro source code to output overland flow. Overland flow depth (m) was converted to overland discharge (m^3 s^{-1}) by multiplying flow depth by grid cell area (10,000 m^2) and dividing by the LSM time step (1 h).

3.4 Channel routing

If overland flow intersects grid cells identified as channel grids [2^{nd} Strahler stream order and above; pre-defined by the hydrologically conditioned USGS National Elevation Dataset 30-m digital elevation model (DEM)], the channel routing module routes the water as channelized streamflow using a 1-dimensional, explicit, variable time-stepping diffusive wave formulation. Similarly, the continuity equation for channel routing is given as:

$$\frac{\partial A}{\partial t} + \frac{\partial Q}{\partial s} = q_l \tag{9}$$

and the momentum equation is given as:

$$\frac{\partial Q}{\partial t} + \frac{\partial (\frac{\gamma Q^2}{A})}{\partial s} + gA\,\frac{\partial H}{\partial s} = -gAS_f \tag{10}$$

where s is the streamwise coordinate, H is water surface elevation, A is the flow cross-sectional area calculated as $(B_w + H\,z)H$ (Fig. B2), q_l is the lateral inflow rate into the channel grid, Q is the flow rate, γ is a momentum correction factor, g is acceleration due to gravity, and S_f is the friction slope computed as:

$$S_f = (\frac{Q}{K})^2 \tag{11}$$

where K is the conveyance computed from the Manning's equation:

$$K = \frac{C_m}{n} AR^{2/3} \tag{12}$$

where n is the Manning's roughness coefficient, A is the channel cross-sectional area, R is the hydraulic radium *(A/P)*, P is the wetted perimeter, and $C_m$is a dimensional constant (1.486 for English units or 1.0 for SI units).

4 Model simulation, calibration, and validation

4.1 Model domain

The WRF-Hydro model domain spans regions in California including the Coast Ranges, Monterey Bay, and the Central Valley, and covers several burn scars from the 2020 wildfire season (Fig. 1a). Here we focus our analysis on the Dolan burn scar where the hazardous debris flows occurred (Fig. 1b). According to the USGS 30-m DEM, the Rat Creek debris flow site sits at the base of a 1^{st} order catchment with a drainage area of 2.23 km^2. Mill Creek, Big Creek, and Nacimiento debris flows were initiated within extremely steep, intensely burned, 1^{st} order catchments, but were deposited in 2^{nd}, 3^{rd}, and 3^{rd} Strahler stream order channels, respectively.

To calibrate and validate WRF-Hydro output, we use soil moisture observations from two Physical Sciences Laboratory (PSL) monitoring stations [i.e., Lockwood (lwd) and Gilroy (gry)] (Fig. 1a).

Due to the Mediterranean climate of California, many USGS stream gages experience low or no flow during the dry season. In addition, many gages are under manual regulation to mitigate wet-season flood risks and better distribute water resources. As such, it can be challenging to obtain natural streamflow observations for model calibration. Here, three USGS stream gages [i.e., Arroyo Seco NR Greenfield, CA (ID 11151870), Arroyo Seco NR Soledad, CA (ID 11152000), and Arroyo Seco BL Reliz C NR Soledad, CA (ID 11152050)] (Fig. 1a) on streams that have measurable flows during our study period and are free of human regulation are used. These gages are located downstream of the Dolan burn scar and hence are useful in calibrating the parameters associated with burn scar effects. The PSL soil moisture observations were recorded at 2-minute intervals and USGS streamflow gage data were recorded at 15-minute intervals, but we perform all observation-model comparisons at hourly-mean resolution.

4.2 Baseline simulation and soil moisture calibration

WRF-Hydro was run from January 1–31 of 2021. We performed the baseline simulation by modifying WRF-Hydro default parameters (Table B3) based on a calibration using soil moisture observations from stations lwd and gry. Neither PSL station is located in a burn scar. Since the baseline simulation includes no postfire characteristics, it can also be regarded as the "pre-fire" scenario. Soil moisture at 10 cm below ground in the baseline simulation was calibrated by performing a domain-wide adjustment of soil porosity and grain size distribution index at the simulation start (Table B3). We then allowed the model to spin up from January 1–10 before using January 11–31 for validation. Using a relatively short spin-up period is justified because prior to the AR event, little rain fell on the Dolan burn scar (i.e., ~400 mm of rainfall fell from June to December 2020). As such, in the months preceding the debris flow events, soil moisture observations indicate already dry condition prior to our 10 day spin up.

After calibration, the simulated soil moisture closely mimics ground-based PSL observations (Fig. 4). Both the observed magnitude and variability are well captured, with the simulated ±1 standard deviation envelope largely encompassing PSL observations during the AR. Model performance was evaluated using four quantitative metrics, i.e., correlation coefficient, root mean square error, mean bias, and Kling-Gupta efficiency (KGE; Gupta et al., 2009; Kling et al., 2012). KGE has previously been used in soil moisture calibration applications (e.g., Lahmers et al., 2019; Vergopolan et al., 2020) and is computed as follows:

$$KGE = 1 - \sqrt{(r-1)^2 + (\alpha-1)^2 + (\beta-1)^2} \tag{13}$$

where r is the correlation coefficient between the observation and simulation, α is the ratio of the standard deviation of simulation to the standard deviation of observation, and β is the ratio of the mean of simulation to the mean of observation. KGEs close to 1 indicate a high-level consistency between the simulation and observation, while negative KGEs indicate poor model performance (Schönfelder et al., 2017; Andersson et al., 2017).

The model's ability to simulate soil moisture substantially improves after calibration (Fig. 4; Table 1). KGE values approach 1 (0.72 at lwd and 0.88 at gry), indicating that WRF-Hydro adequately simulates the hydrologic environment and its response to meteorological change.

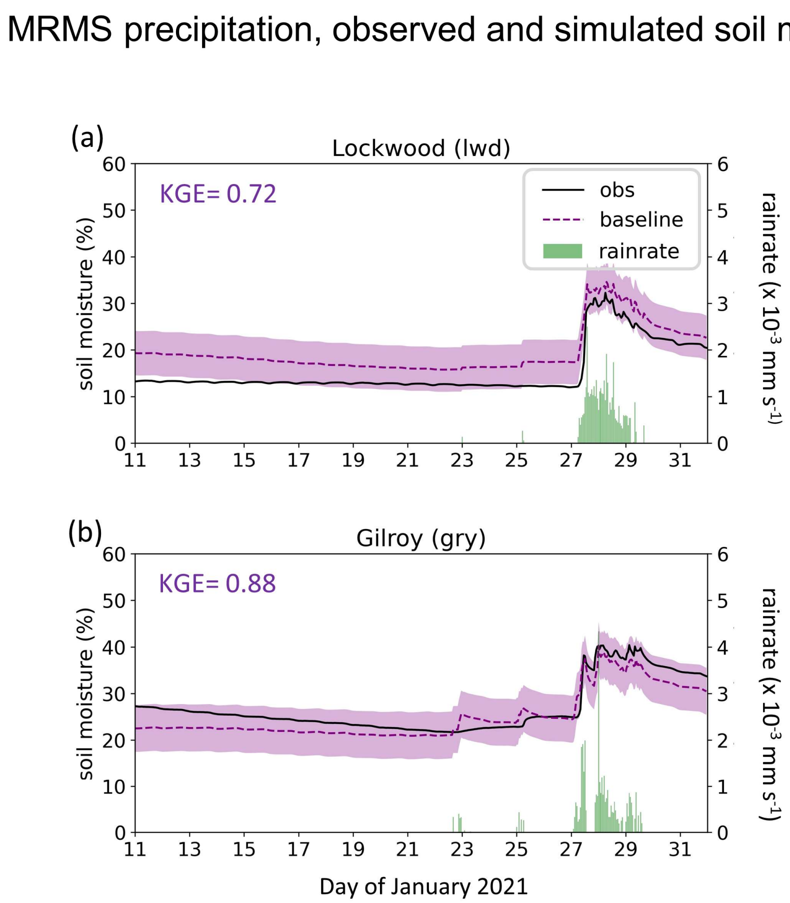

Fig. 4| Precipitation, observed and simulated soil moisture at two PSL soil moisture stations. January 11–31, 2021 MRMS precipitation (green bars) and observed (black line) and simulated volumetric soil moisture 10 cm below ground in the baseline simulation (purple dashed line) at PSL sites (a) Lockwood (lwd) and (b) Gilroy (gry). Envelope of purple shading depicts ±1 standard deviation of model simulated soil moisture. KGE scores are provided at top left for each station.

Table 1
Evaluation metrics of simulated soil moisture and streamflow

Soil moisture (Default / Baseline)				
Station	***r***	**RMSE**	**Bias**	**KGE**
lwd	0.97 / 0.98	7.06 / 4.32	5.21 / 4.16	0.10 / 0.72
gry	0.94 / 0.94	5.19 / 2.53	-4.79 / -1.66	0.80 / 0.88
Streamflow (Baseline / Burn scar)				
Station	***r***	**RMSE**	**Bias**	**NSE**
1870	0.28 / 0.93	39.29 / 14.69	1.65 / 3.36	-0.17 / 0.84
2000	0.26 / 0.86	51.22 / 24.92	2.47 / 4.81	-0.15 / 0.73
2050	0.25 / 0.81	49.96 / 27.43	5.70 / 8.24	-0.38 / 0.53

Table 1| Quantitative evaluation metrics for the simulated soil moisture and streamflow when compared against observations. The metrics include the Pearson correlation coefficient (r), root mean square error (RMSE), and mean bias (Bias). In addition, the comprehensive metrics Kling-Gupta efficiency (KGE) and Nash-Sutcliffe efficiency (NSE) are used to evaluate model-simulated soil moisture and streamflow, respectively. For soil moisture, the numbers in front of "/" are calculated between the default run (i.e., uncalibrated run) and the observations, whereas the numbers following "/" are the corresponding values in the baseline simulation (the purple dashed line in Fig. 4). For streamflow, the numbers in front of "/" are computed between the baseline run (purple dashed line in Fig. 6) and the observations, while the numbers behind "/" are for burn scar simulation (red line in Fig. 6). If the model performance regarding a certain metric is enhanced in the burn scar simulation, the number after "/" is underlined.

4.3 Burn scar simulation and streamflow calibration

To simulate effects of wildfire burn scars on hydrologic processes and debris flow hazards, we made two modifications to the baseline simulation soil moisture calibrated model configuration. First, we changed the land cover type within the burn scar perimeter to its nearest LSM analogue, i.e., "barren and sparsely vegetated". The switch to barren land causes: (1) height of the canopy (HVT) to decrease to 0.5 m; (2) maximum rate of carboxylation at 25°C (VCMX25) to decrease to 0 $\mu mol\ CO_2/(m^2 \cdot s)$; and (3) overland flow roughness coefficient (OV_ROUGH2D) to decrease to 0.035 (Fig. 5a–c) from default values (Fig. B4 and Table B2).

The second adjustment was to decrease soil infiltration rates within the burn scar perimeter, achieved by reducing soil saturated hydraulic conductivity (DKSAT; Fig. 5d; Scott & van Wyk, 1990; Cerdà, 1998; Robichaud, 2000; Martin & Moody, 2001) from default values (Table B3). Consistent with the hydrophobicity of burned soils, we calibrate the burn scar simulation by systematically exploring a range of burn scar area saturated hydraulic conductivities (0 to 3×10^{-7} m s^{-1} with a 5×10^{-8} m s^{-1} increment), with the goal of reproducing streamflow behavior similar to USGS gage observations. We found that a value of 1.5×10^{-7} m s^{-1} gives the highest Nash-Sutcliffe efficiency (NSE; Nash & Sutcliffe, 1970) across all three USGS stream gages (Table 1). NSE and KGE are the two most widely used metrics for calibration and evaluation of hydrologic models. The NSE has previously been used in streamflow calibration applications (e.g., Xia et al., 2012; Bitew & Gebremichael, 2011), and it is calculated as follows:

$$NSE = 1 - \frac{\sum_{t=1}^{t=T}(Q_{sim}(t)-Q_{obs}(t))^2}{\sum_{t=1}^{t=T}(Q_{obs}(t)-\overline{Q_{obs}})^2} \tag{14}$$

where T is the length of the time series, $Q_{sim}(t)$ and $Q_{obs}(t)$ are the simulated and observed discharge at time t, respectively, and $\overline{Q_{obs}}$ is the mean observed discharge. By definition, NSEs of 1 indicate perfect correspondence between the simulated and observed streamflow. Positive NSEs mean that the model streamflow has a greater explanatory power than the mean of the observations, whereas negative NSEs represent poor model performance (e.g., Moriasi et al., 2007; Schaefli & Gupta, 2007). When burn scar characteristics are included, NSEs increase from negative values in the baseline to greater than 0.5, and the NSEs at gages 1870 and 2000 reach 0.84 and 0.73, respectively. Higher NSE scores indicate the abovementioned burn scar parameter changes improve the model's ability to simulate streamflow observations downstream of the burn scar (Table 1).

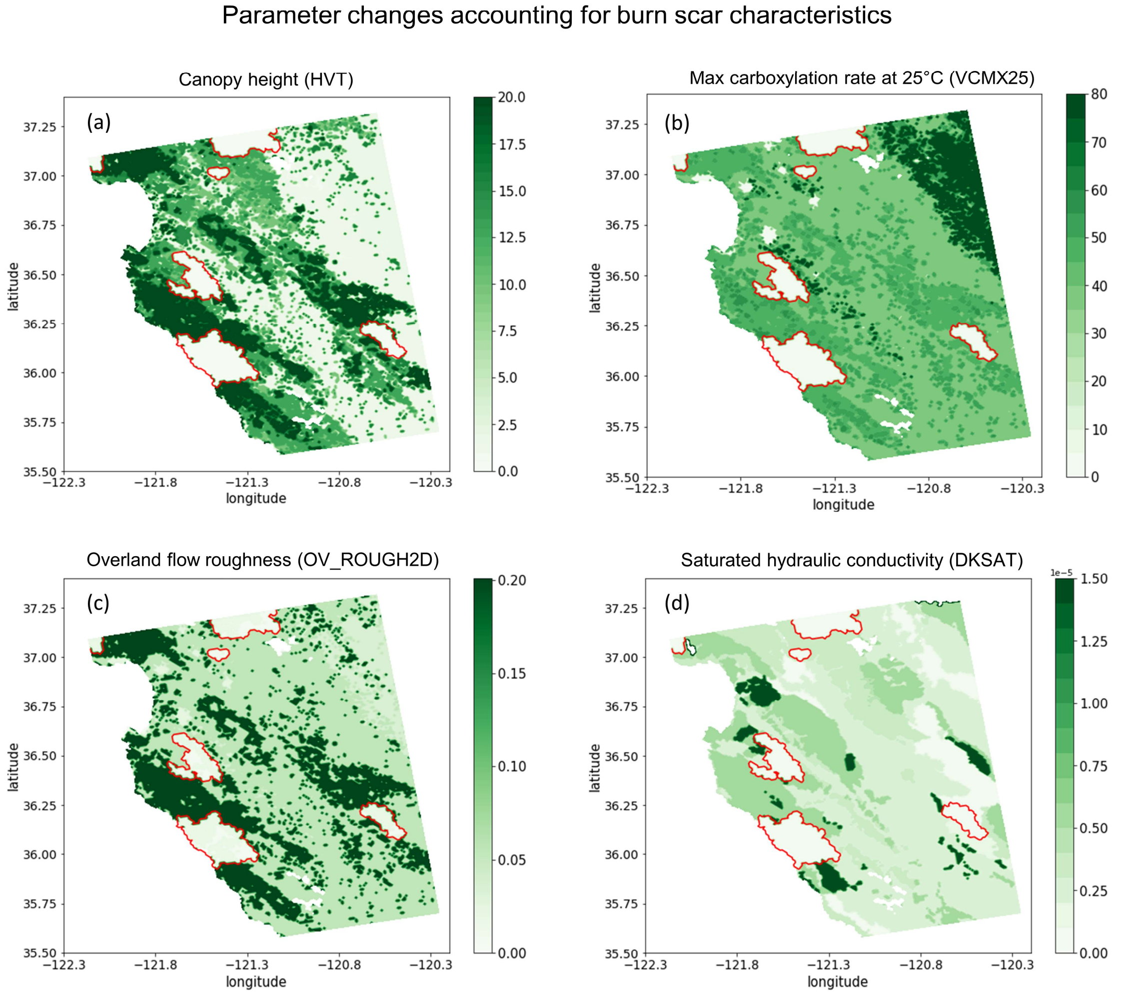

Fig. 5| Parameter setting in the WRF-Hydro burn scar simulation. (a) The height of the canopy (HVT; m; shading), (b) maximum rate of carboxylation at 25°C (VCMX25; $\mu mol\ CO_2/(m^2 \cdot s)$; shading), (c) overland flow roughness coefficient (OV_ROUGH2D; shading), and (d) saturated hydraulic conductivity (DKSAT; m s^{-1}; shading) in the burn scar simulation.

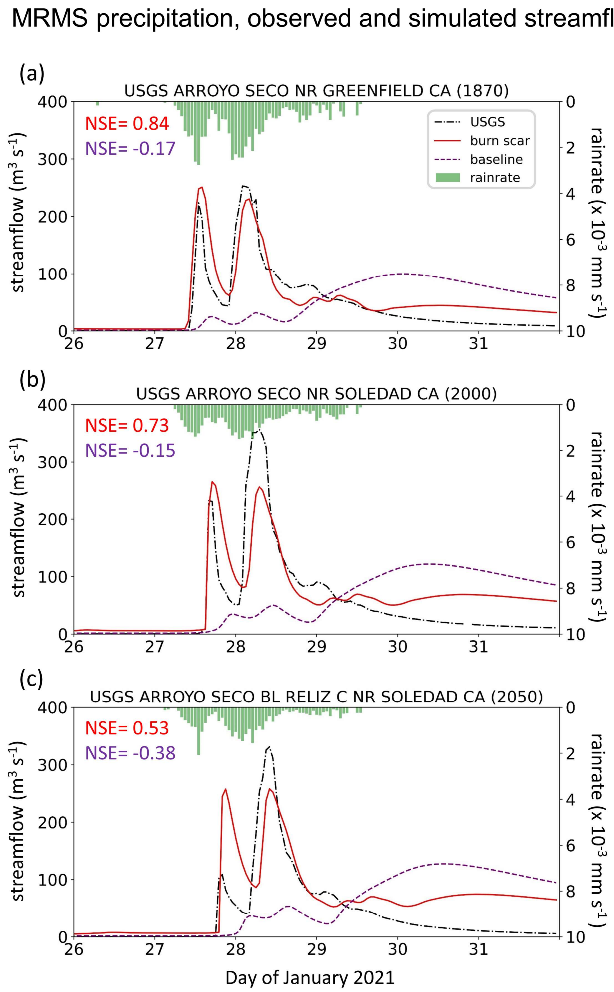

Fig. 6| Precipitation, observed and simulated streamflow at three USGS stream gages. January 26–31, 2021 MRMS precipitation (green bars), observed (black dash dotted line) and simulated streamflow in baseline simulation (purple dashed line) and burn scar simulation (red line) at (a) Arroyo Seco NR Greenfield, CA (ID 11151870), (b) Arroyo Seco NR Soledad, CA (ID 11152000), and (c) Arroyo Seco BL Reliz C NR Soledad, CA (ID 11152050). NSE scores for baseline (purple) and burn scar simulations (red) are shown at top left.

5 Results

5.1 Hydrologic response due to burn scar incorporation

The pre-fire baseline simulation fails to capture the hydrologic behavior observed at the USGS gages located within the burn scar (Fig. 6). Incorporation of burn scar characteristics substantially alters the hydrologic response of the model and provides much higher fidelity streamflow simulations (Fig. 6). Observed hydrographs are characterized by two early streamflow peaks related to two precipitation bursts on January 27^{th} and 28^{th}. Our burn scar simulation captures this behavior, while the baseline simulation streamflow peaks just once, with a lower magnitude and an ~3-day lag after peak precipitation (Fig. 6). The steep rising limbs and high magnitude discharge peaks of the burn scar hydrograph are indicative of flash flooding. Compared with the pre-fire baseline scenario, the burn scar's barren land and low infiltration rate substantially accelerate drainage rates and increase discharge volume into stream channels.

5.2 Hydrologic response at four debris flow sites

We identified locations and extent of four debris flows from remote sensing data and field work (Fig. 3& Fig. B1). rdNDVI shows vegetation loss caused by debris flows. Mill Creek, Big Creek, and Nacimiento were relatively large debris flows with runout lengths between ~2–5 km. Rat Creek occurred in a smaller catchment and had a runout length of ~300 m. The difference in runout length and debris flow size is primarily controlled by upstream catchment size. Due to its low stream order (1^{st} Strahler stream order), Rat Creek is the only debris flow site modeled entirely as overland flow in our WRF-Hydro simulations.

At the four debris flow sites, we use three metrics to characterize hydrologic anomalies: (1) accumulated runoff volume, (2) peak discharge, and (3) time to peak discharge. Fig. 7 depicts accumulated channelized discharge volume (blue shading) and accumulated overland discharge volume (yellow-red shading) from January 27^{th} 00:00 to 28^{th} 12:00 near the four debris flow sites in the burn scar simulation. Accumulation time period is chosen such that it covers the first two runoff surges in the simulated hydrographs which are likely associated with debris flows (Fig. 8) given that nearly concurrent peak rainfall intensity and peak discharge is a signature characteristic of debris flows (Kean et al., 2011). Runoff volume is on the order of 10^4 m^3 at Rat Creek and 10^6 m^3 at the other three sites.

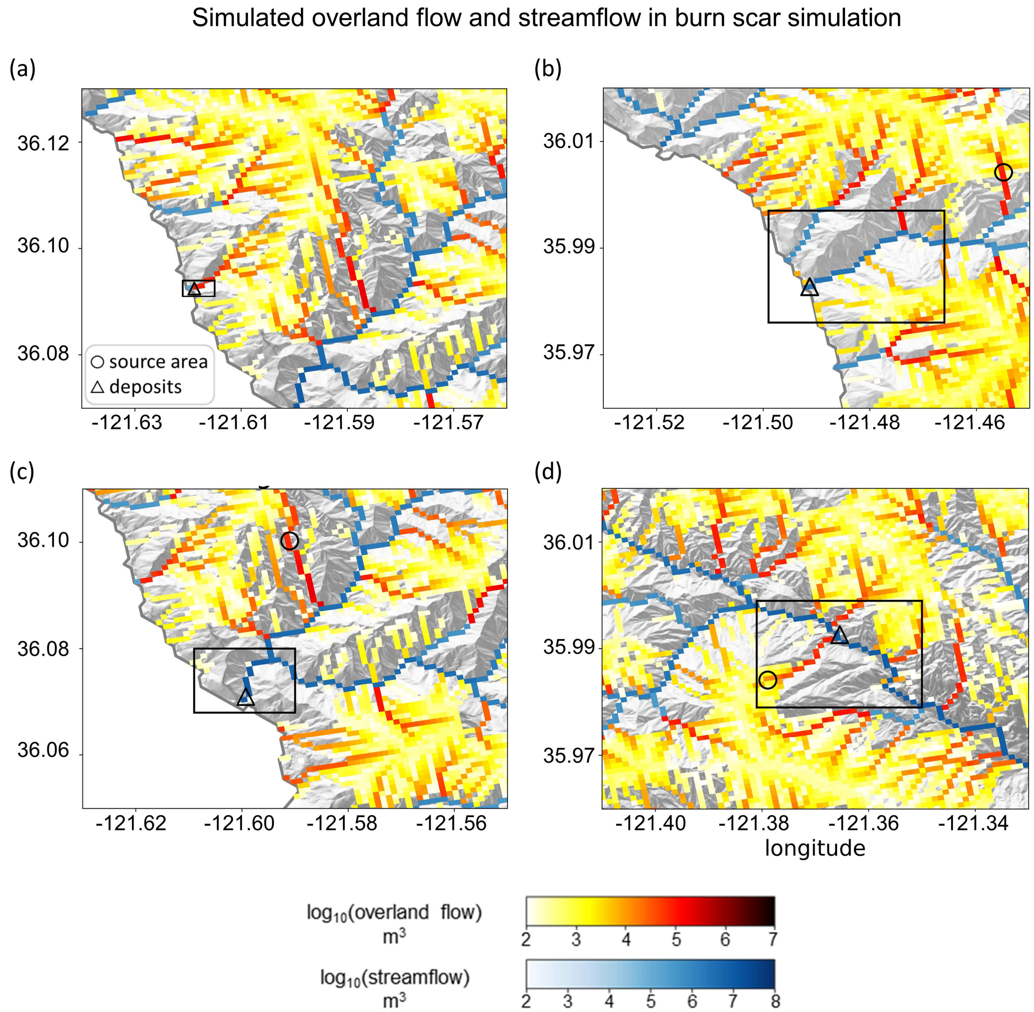

Fig. 7| WRF-Hydro simulated overland flow and streamflow in the burn scar simulation. (a)–(d) Total volume of accumulated overland flow (yellow-red shading) and streamflow (blue shading) on *log*$_{10}$ scale between January 27th 00:00 and 28th 12:00 at four debris flow sites. Black rectangles correspond to domains in Fig. 3a–d. Black circles and triangles indicate debris flow source areas and deposits, respectively.

Dramatic hydrographic changes after inclusion of burn scar characteristics are simulated at debris flow source areas (Fig. B6 and Table B4) and deposition sites (Fig. 8 and Table 2). WRF-Hydro facilitates investigation of the hydrologic response at triggering and deposition locations and along the runout path. Here, to emphasize the downstream hazards, our analysis is focused on debris flow deposits. At Rat Creek, where a section of CA1 collapsed, the magnitude of discharge substantially increases, and overland flow surges are concurrent with rainfall bursts (Fig. 8a). Total discharge accumulated during the AR event increases approximately eight-fold (791%), and peak discharge more than triples compared to the baseline simulation (Fig. 8a and Table 2). At Mill Creek, Big Creek, and Nacimiento, baseline hydrographs are characterized by less variability, muted responses to two early precipitation bursts, and a delayed third discharge peak that does not occur until ~3 days after AR passage (Fig. 8b–d). Maximum discharge peaks in the baseline hydrographs lag those in the burn scar simulation by ~2 days (Fig. 8b–d; Table 2). In the burn scar simulation, total volume substantially increases at the three channelized sites – total volume increases ~650% at Mill Creek, ~891% at Big Creek, and ~829% at Nacimiento (Fig. 8b–d and Table 2), and the absolute increase in volume is on the order of 10^6 m^3 (Table 2). Peak discharge more than triples at Mill Creek and Big Creek and more than quadruples at Nacimiento. Additionally, response times of the peak in discharge to the peak in precipitation decrease to less than an hour, highlighting the simulated flashiness of the burned catchments.

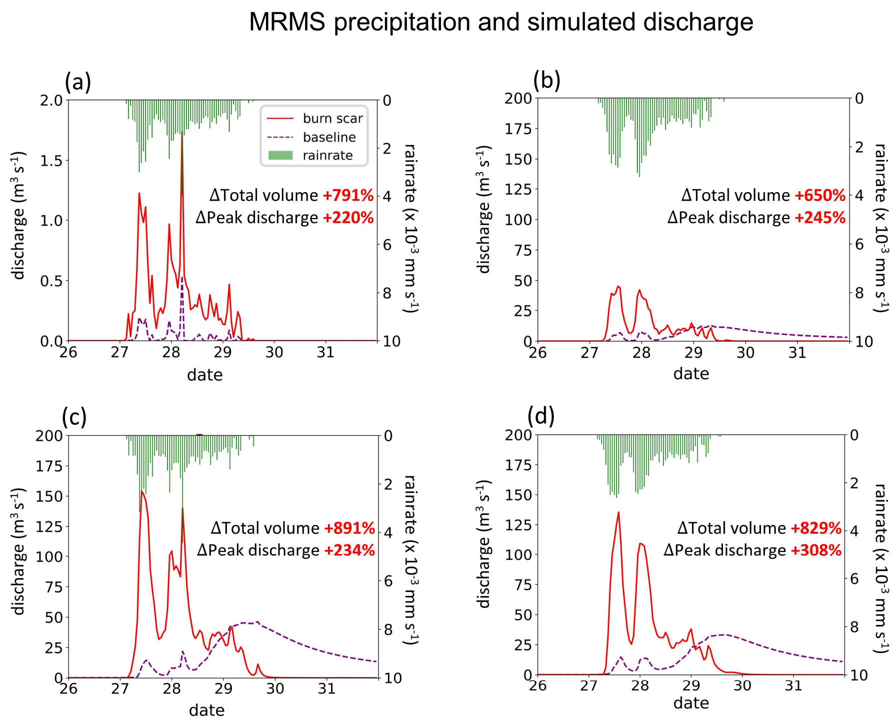

Fig. 8| WRF-Hydro simulated discharge time-series at four debris flow deposition locations. (a)–(d) MRMS precipitation (green bars) and simulated discharge time-series for January 26th 00:00 to 31st 23:00 at (a) Rat Creek, (b) Mill Creek, (c) Big Creek, and (d) Nacimiento deposition locations (black triangles in Fig. 7a–d) in baseline simulation (purple dashed line) and burn scar simulation (red line).

Table 2
The total runoff volume, peak discharge, and peak timing at debris-flow deposits

Site name	Baseline simulation			Burn scar simulation			
	Total volume (m^3)	Peak discharge ($m^3\ s^{-1}$)	Highest peak timing	Total volume (m^3)	Peak discharge ($m^3\ s^{-1}$)	1st Peak timing	2nd Peak timing
Rat Creek	6,897	0.54	28th 05:00	61,425 (+791%)	1.73 (+220%)	27th 09:00	28th 05:00
Mill Creek	312,925	13.10	29th 08:00	2,347,457 (+650%)	45.21 (+245%)	27th 13:00	27th 23:00
Big Creek	842,808	46.10	29th 16:00	8,354,095 (+891%)	154.10 (+234%)	27th 10:00	28th 05:00
Nacimiento	743,531	33.15	29th 16:00	6,904,706 (+829%)	135.41 (+308%)	27th 14:00	28th 00:00

Table 2| The total runoff volume, peak discharge, and peak timing in the baseline and burn scar simulations from January 27th 00:00 to 31st 23:00 at deposition sites of Rat Creek, Mill Creek, Big Creek, and Nacimiento debris flows (black triangles in Fig. 7a–d). The peak timing shown in the baseline simulation is for the highest peak. The percent change of the total volume and peak discharge in the burn scar simulation relative to the baseline simulation are shown in parentheses.

5.3 Debris flow hazard assessment for the Dolan burn scar

Since high magnitude runoff is often the cause and precursor of runoff-generated debris flows in burned areas (Cannon et al., 2003, 2008; Rengers et al., 2016), we use simulated accumulated volume of overland flow and streamflow to assess runoff-generated debris flow hazard potential under pre-fire (i.e., baseline; Fig. 9a&d) and postfire (i.e., burn scar simulation; Fig. 9b&e) conditions. We assess changes at both stream and catchment levels and use the difference between burn scar and baseline simulations to assess added debris flow hazard potential (Fig. 9c&f). Consistent with the increasing erosive and entrainment power associated with increasing discharge, our debris flow hazard increases as the accumulated discharge volume increases. To reduce the effects of catchment size on the volume-based hazard levels, we normalize a catchment's discharge volume by the area of the catchment (Santi et al., 2012; Fig. 9d–f). Non-normalized catchment hazard maps are also provided (Fig. B7).

In the pre-fire baseline simulation, the AR-induced precipitation produces lower debris flow hazard over most of the domain, but elevated hazards along stream channels (Fig. 9a). We note no substantial differences between areas in or out of the burn scar. In the burn scar simulation, debris flow hazard levels increase across the Dolan burn scar and along channels outside but downstream of the burn scar (Fig. 9b–c). The discharge volume increases by an order of magnitude near Rat Creek, Big Creek, Mill Creek, and Nacimiento. Within the burn scar, hazards along major stream channels, such as the Nacimiento River and San Antonio River increase. Outside the burn scar, hazard levels along river channels downstream of the burn scar, such as the Arroyo Seco River, also increase (Fig. 9c).

At the catchment level, debris flow hazards are assessed using accumulated discharge volumes normalized by catchment areas (Fig. 9d–f). Accumulated discharge volumes are assessed at the outlet of each catchment between January 27th 00:00 to 28th 12:00. In the baseline simulation, the majority of catchments are subject to relatively low debris flow hazards compared to the burn scar simulation with total normalized discharge volume less than 10^3 m^3 km^{-2} (Fig. 9d). In the burn scar simulation, over half of catchments within the Dolan burn scar have normalized discharge volume greater than 10^5 m^3 km^{-2}, while over 1/4 of basins reach 10^6 m^3 km^{-2} (Fig. 9e). The additional debris flow hazard brought about by the inclusion of wildfire burn scar characteristics is substantial (Fig. 9f).

To summarize changes in debris flow hazards as a result of including burn scar characteristics in WRF-Hydro simulations, we create distributions of pre-fire baseline and burn scar catchment-area normalized discharge from the 404 catchments located within the Dolan burn scar perimeter (Fig. 10). After incorporating burn scar characteristics, the full distribution shifts to the right, indicating increased hazard levels – a shift considered robust by a Student's t-test (p value: 4.6E-45). A quantitative assessment of this shift indicates that the mean catchment area normalized discharge volume increases by ~1300% (from ~380k to 5.5M m^3 km^{-2}) while the standard deviation increases ~1400% (from ~1.6M to 23.0M m^3 km^{-2}). We also assess shifts at a range of distribution percentiles: 5P: 148% (~0.6k to ~1.5k m^3 km^{-2}), 25P: 725% (~3.7k to ~30.7k m^3 km^{-2}), 50P: 924% (~13k to ~135k m^3 km^{-2}), 75P: 980% (~120k to ~1.3M m^3 km^{-2}), and 95P: 1300% (~2.1M to ~29.1M m^3 km^{-2}). In the burn scar simulation, more than half of catchments have normalized volumes > 10^5 m^3 km^{-2} and more than 1/4 of catchments have volumes > 10^6 m^3 km^{-2} – values that correspond to the 75P and 90P of the baseline simulation, respectively. Disproportionate shifting of the right tail of the distribution suggests that extreme debris flow hazards increase non-linearly under simulated burn scar conditions.

Our catchment-area normalized discharge volume-based hazard assessment also indicates that the catchments containing Mill Creek, Big Creek, and Nacimiento had elevated hazard potential (Fig. 9d–f), consistent with our (limited) debris flow observations. Other areas with elevated hazards include catchments containing the Arroyo Seco and San Antonio Rivers. Beyond the burn scar perimeter, effects of fire expand to adjacent and downstream catchments, and the drainage basins of the Arroyo Seco and Nacimiento Rivers are simulated to have potentially hazardous conditions, i.e., normalized discharge volumes in excess of 10^6 m^3 km^{-2} (Fig. 9e&f).

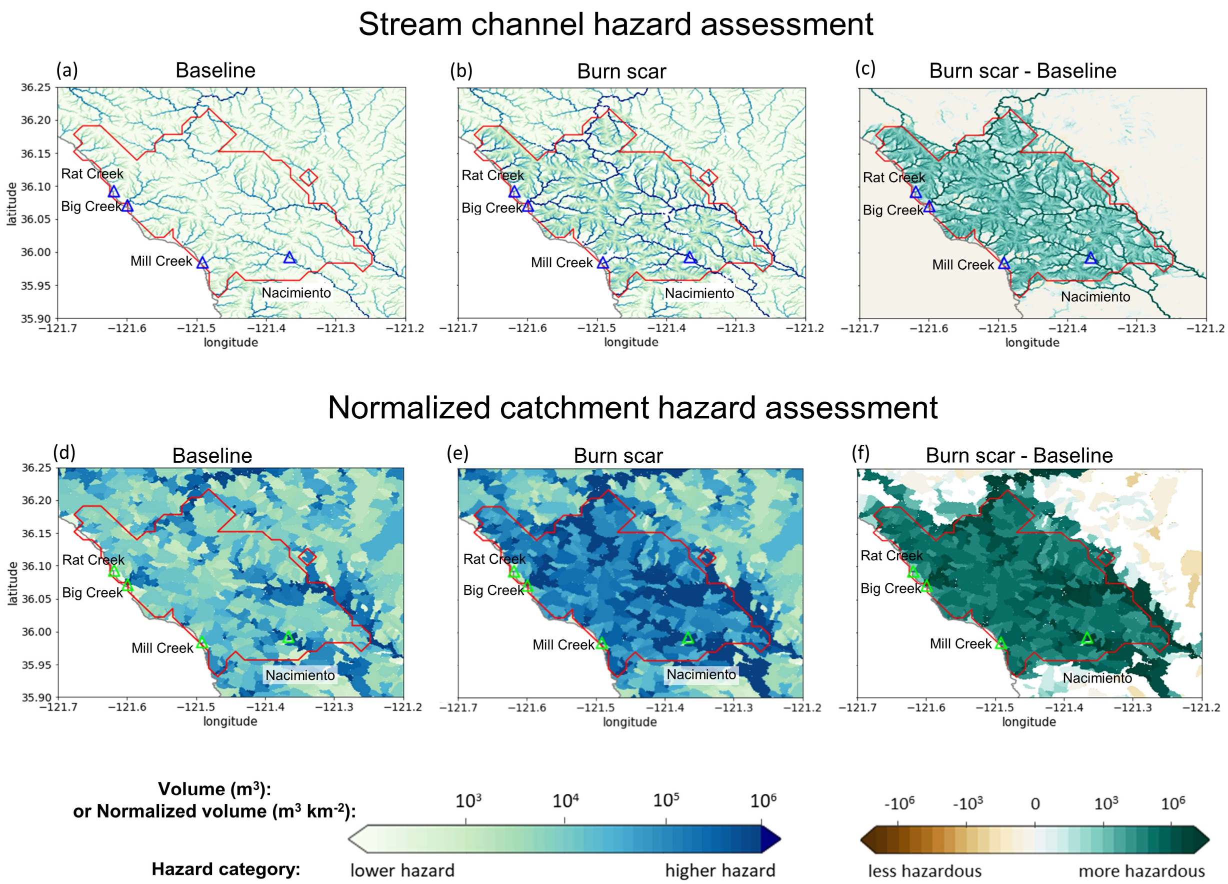

Fig. 9| Discharge volume-based runoff-generated debris flow hazards. Debris flow hazards at individual stream level for the (a) baseline, (b) burn scar, and (c) difference between burn scar and baseline simulations. Hazard is estimated as total discharge volume from January 27th 00:00 to 28th 12:00. (d)–(f) Normalized debris flow hazards by catchment area at catchment level. For each catchment, the hazard is determined by total discharge volume at the catchment outlet from January 27th 00:00 to 28th 12:00 divided by catchment area.

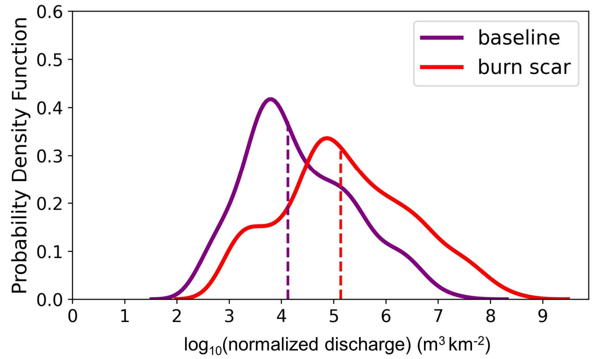

Fig. 10| Distributions of accumulated discharge volumes at the outlet of the 404 catchments normalized by upstream catchment areas within Dolan burn scar in the baseline simulation (purple line) and in the burn scar simulation (red line). Dashed vertical lines indicate median values.

5.4 Debris flow hazard assessment at regional scales

While the results we present above primarily focus on hazards in the Dolan burn scar, our WRF-Hydro domain includes a number of additional 2020 wildfire burn scar sites (Fig. 1a). Given the long filament-like structure of western U.S. landfalling ARs, the heterogeneous nature of landfalling trajectories, and the potential for systems to interact with diverse topographic terrains, the development of tools capable of regional hazard assessments under high-gradient precipitation events is crucial – particularly in a wildfire-prone region like California. To demonstrate the potential utility of WRF-Hydro in regional applications, we assess hazards over our full domain (Fig. 11). We find that hazard potential, from both channelized and overland flows, is greatest within the burn scar sites, with maximum hazards found in the Dolan burn scar, consistent with the location of elevated precipitation along the Coast Ranges – where more than 300 mm of rain fell over three days (Fig. 11). Other high hazard-elevated precipitation regions within our domain include the western edge of the Sierra Nevada and areas north of Monterey Bay, which collocate with the Mineral and Del Puerto burn scars, respectively. Similar to our Dolan burn scar focused analysis, areas within and downstream of these burn scar sites have elevated streamflow discharge volumes compared to the non-burned areas (Fig. 11b). Likewise, areas of heightened accumulated overland flow are elevated in burn scar regions, but also demonstrate a strong correspondence to the spatial distribution of precipitation (Fig. 11a & c).

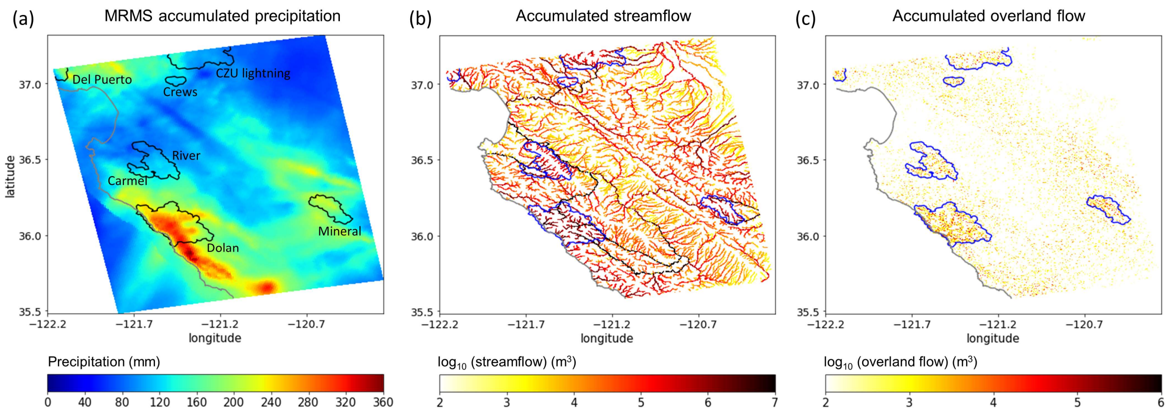

Fig. 11| MRMS accumulated precipitation and regional debris flow hazard assessment. (a) MRMS accumulated precipitation during January 27th 00:00 to 29th 23:00 over the model domain (shading; mm). Names of burn scars are labeled in black. (b) Accumulated streamflow (yellow-to-red shading; m^3) and (c) accumulated overland flow from 27th 00:00 to 28th 12:00 over the model domain (yellow-to-red shading; m^3). Wildfire perimeters of 2020 wildfire season are outlined in black in (a), and in blue in (b) and (c). The coastline of California is in grey.

6 Discussion

Given the historic and growing frequency of wildfires in the western U.S. (Swain 2021; Williams et al., 2019; Goss et al., 2020) and globally (Jolly et al., 2015; Flannigan et al., 2013), developing tools to investigate, better understand, and potentially predict changes in burn scar hydrology and natural hazards at regional scales is critical. Here, we demonstrate the first use of WRF-Hydro to simulate the surface hydrologic response over a burn scar during a landfalling AR. We augmented the default version of WRF-Hydro to output overland flow and to replicate burn scar behavior by adjusting vegetation type and infiltration rate parameters. WRF-Hydro simulations were validated against PSL soil moisture and USGS streamflow observations before we used simulated streamflow and overland flow volumes to characterize debris flow hazard potential.

A comparison between baseline and burn scar simulations demonstrated that changes in hydraulic properties of burned areas causes drastic changes in surface flows, including faster discharge response times, greater discharge volumes, and overall flashier hydrologic behavior in surface flows. As a result of including bur scar characteristics in WRF-Hydro simulations, median catchment-area normalized discharge volume increases nine-fold, while 95P volume increases 13-

fold. The magnitude of our simulated changes is consistent with findings from previous postfire hydrology studies (Anderson et al., 1976; Scott, 1993; Meixner & Wohlgemuth, 2003; Kinoshita & Hogue, 2015; Kean et al., 2011). At Rat Creek, where a debris flow destroyed CA1, our model simulation predicted an eight-fold increase in accumulated overland flow and a tripling in peak discharge when compared to the baseline simulation. At Mill Creek, Big Creek, and Nacimiento, the increase of runoff volume from the baseline to the burn scar simulation is on the order of 10^6 m^3. Our hazard assessments based on catchment-area normalized discharge volumes indicated that Mill Creek, Big Creek, and Nacimiento were under elevated debris flow hazards, corresponding well with identified debris flow occurrences.

Despite methodological differences, our debris flow hazard assessment for this AR event is generally consistent with the USGS' postfire, pre-AR, design-storm-based preliminary hazard assessment (USGS, 2020). As described above, USGS preliminary hazard assessments use logistic regression models to estimate the likelihood of debris flow occurrence and multivariate linear regression models to estimate debris flow volumes. This empirical approach is trained on historical western U.S. debris flow occurrence and magnitude data and incorporates estimated burn scar soil erodibility and burn severity data (Cannon et al., 2010; Gartner et al., 2014; Staley et al., 2016). For precipitation, the USGS assessment utilizes a design storm approach that assumes 1–5 year return interval magnitude precipitation falls uniformly over a region/burn scar (USGS, 2020). For the Dolan burn scar, both assessments find that large stream channels had relatively higher hazard levels than small streams or overland areas. However, close comparison of hazard maps reveals differences in spatial distribution of high-hazard catchments. In the USGS assessment, higher hazard levels are predicted north and southeast of the burn scar, whereas in our assessment the highest hazards occur along major stream channels. We hypothesize that USGS-assessed areas of higher hazard potential are related to their use of design-storm precipitation (see Fig. 2 for MRMS precipitation footprint) and burn severity data (Burned Area Emergency Response, 2020). Comparison with the USGS assessment framework suggests room for improvement in WRF-Hydro-based assessments (i.e., inclusion of burn severity and soil erodibility data), but also highlights the potential utility of working with spatially-distributed and time-varying precipitation. However, this also means the accuracy of WRF-Hydro predictions depends on the accuracy of precipitation forcing, and in our hindcast application, MRMS precipitation data (Appendix A). Accordingly, our WRF-Hydro-based hazard assessment could benefit from precipitation products mosaiced from various sources to constrain precipitation-based uncertainties (e.g., gauge-corrected and/or Mountain Mapper MRMS), although the long processing time of these datasets inhibits timely post-event assessments.

As a water-only model, WRF-Hydro is currently restricted to simulating the hydrologic ingredients of debris flows. While water-only models have been widely used to investigate and better understand debris flow dynamics (Arattano & Savage, 1994; Arattano & Franzi, 2010; Rengers et al., 2016; McGuire & Youberg, 2020; Di Cristo et al., 2021), sediment supply, soil erodibility, and other sedimentological factors also play important roles in determining the potential for and severity of mass failure events (McGuire et al., 2017). Developing a debris flow model that couples hydrologic and sediment erosion and transport processes would represent a significant advance and be of great practical use (Banihabib et al., 2020; Shen et al., 2021). At a minimum, soil grain size maps and domain-specific rainfall intensity-duration curves can provide guidance to define transitions from water floods to debris flows if historical debris flow data is available in the study domain (McGuire & Youberg, 2020; Tognacca et al., 2000; Gregoretti & Fontana, 2008; Cannon et al., 2007).

7 Conclusion

Use of WRF-Hydro to simulate runoff-generated debris flow hazards in burn scar settings represents a novel application. It is notable that in this application we have balanced the computational cost of a regional domain with our choice of resolved spatial resolution for terrain routing and overland flow calculations (100 m). However, WRF-Hydro has previously been applied to smaller domains at higher terrain routing resolutions (~30 m). Future work could assess the use of the model to study burn scar hydrology at finer spatial scales, should the application warrant and should underlying data at sufficient resolution exist. Other potential applications of our modified model framework include alpine areas and steep hillslopes with sparse vegetation where runoff-generated debris flows dominate over landslide-initiated ones (Davies et al., 1992; Coe et al., 2003, 2008).

Further, our burn scar parameter changes are performed to Noah-MP, which is the core land surface component of the National Centers for Environmental Prediction Global Forecast System (GFS) and Climate Forecast System (CFS), thus the findings presented herein, are likely to prove useful in the broader worlds of forecast meteorology and climate science. In addition, here WRF-Hydro is driven by historical precipitation and meteorological data, i.e., in hindcast mode. We see no reason why this modeling framework could not also be employed to project hazards under future climatic conditions (e.g., Huang et al., 2020), or given its relatively low computational expense, in operational forecast mode. Indeed, modern ensemble-based meteorological forecasting could provide high spatiotemporal forcing data with which disaster preparedness managers could probabilistically assess debris flow hazard potential, and issue advanced life and property saving warnings.

Appendix A

Text A1. Multi-Radar/Multi-Sensor System (MRMS) radar-only precipitation estimate and uncertainty

MRMS is a precipitation product that covers the contiguous United States (CONUS) on 1-km grids. It combines precipitation estimates from sensors and observational networks (Zhang et al., 2011, 2014, 2016), and is produced at the National Centers for Environmental Prediction (NCEP) and distributed to National Weather Service forecast offices and other agencies. Input datasets used to produce MRMS include the U.S. Weather Surveillance Radar-1988 Doppler (WSR-88D) network and Canadian radar network, Parameter-elevation Regressions on Independent Slopes Model (PRISM; Daly et al. 1994, 2017), Hydrometeorological Automated Data System (HADS) gauge data with quality control (Qi et al., 2016), and outputs from numerical weather prediction models. There are four different MRMS quantitative precipitation estimates (QPE) products incorporating different input data or combinations: radar only, gauge only, gauge-adjusted radar, and Mountain Mapper. For our study period (i.e., January 1–31, 2021), only the radar-only QPE is currently available.

We acknowledge that precipitation data has uncertainties. Use of different precipitation products may produce different results. A study comparing different gridded precipitation datasets including satellite-based precipitation data, gauge dataset, and multi-sensor products revealed large uncertainties in precipitation intensity (Bytheway et al., 2020). However, comparing different precipitation datasets to characterize uncertainties is beyond the scope of this study. MRMS provides gridded precipitation at high temporal (hourly) and spatial (1-km) resolutions, making it a useful tool to demonstrate the utility of WRF-Hydro in post-wildfire debris flow hazard assessments.

Appendix B

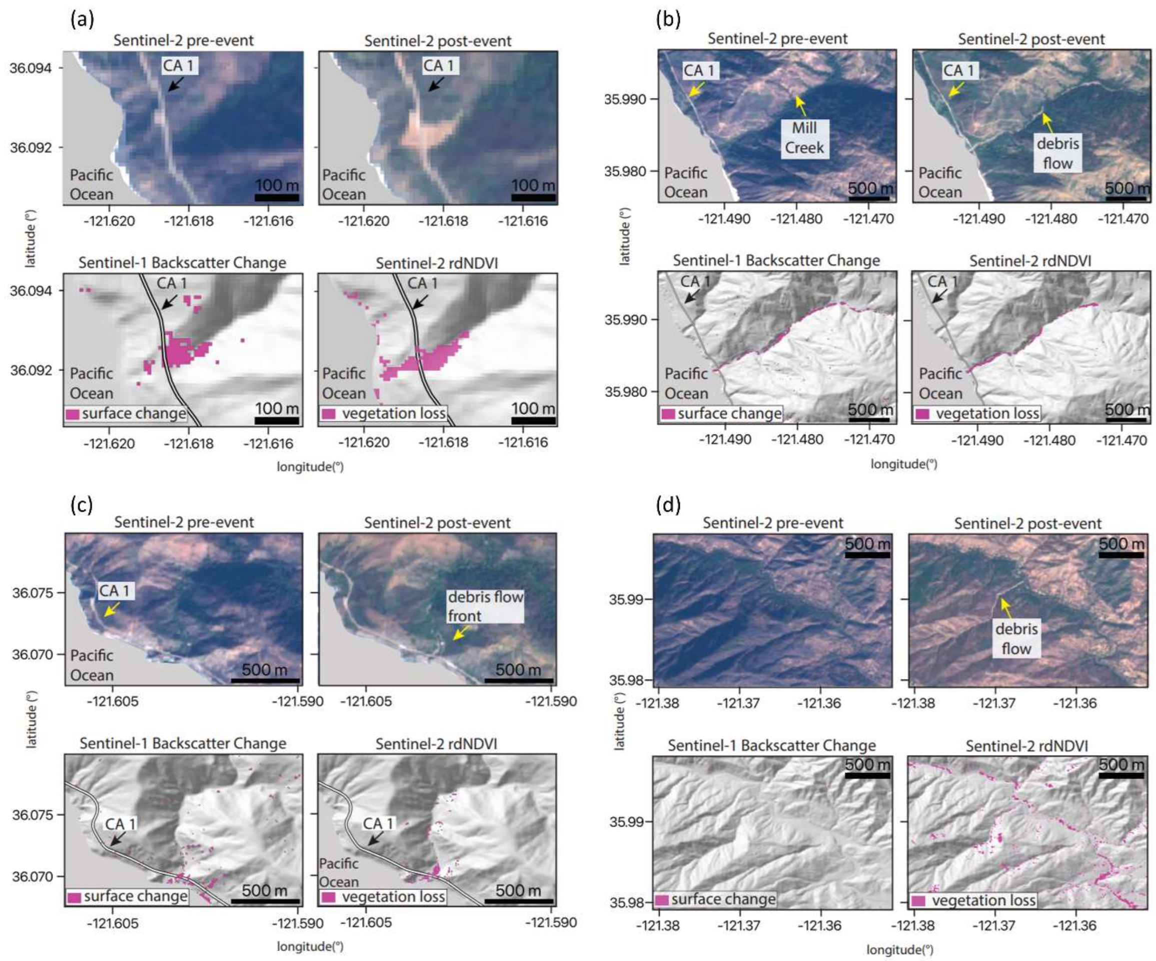

Fig. B1 Optical- and SAR-based remote sensing data of four debris flows. Optical data from Sentinel-2 show pre- and post-debris flow imagery in real color. rdNDVI calculated from the Sentinel-2 data show a decrease in vegetation corresponding to debris flow locations. Sentinel-1 backscatter change shows the change in ground surface properties determined by calculating the log ratio of pre- and post-event SAR images. The pre-event, post-event satellite images, Sentinel-1 Backscatter, and Sentinel-2 rdNDVI change at (a) Rat Creek, (b) Mill Creek, (c) Big Creek, and (d) Nacimiento.

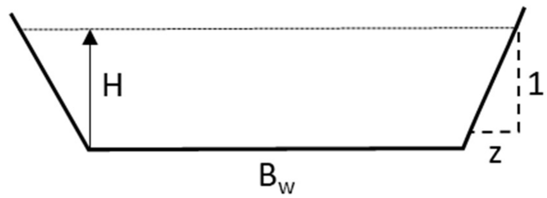

Fig. B2 Schematic trapezoidal shape and related parameters of channels in WRF-Hydro. B_w is the channel bottom width (m), z is the channel side slope (m), and H is water elevation (m). The cross-sectional area of flow is calculated as $(B_w + H\ z)H$.

Table B1 Parameters of trapezoidal channels in WRF-Hydro.

Stream order	Channel bottom width B_w (m)	Channel side slope z (m)	Manning's roughness coefficient n
1	1.5	3	0.33
2	3	1	0.21
3	5	0.5	0.09
4	10	0.18	0.06
5	20	0.05	0.04
6	40	0.05	0.03
7	60	0.05	0.02
8	70	0.05	0.02
9	80	0.05	0.01
10	100	0.05	0.01

Table B1 Parameters of the trapezoidal channels in WRF-Hydro including channel bottom width B_w (m), channel side slope z (m), and Manning's roughness coefficient n.

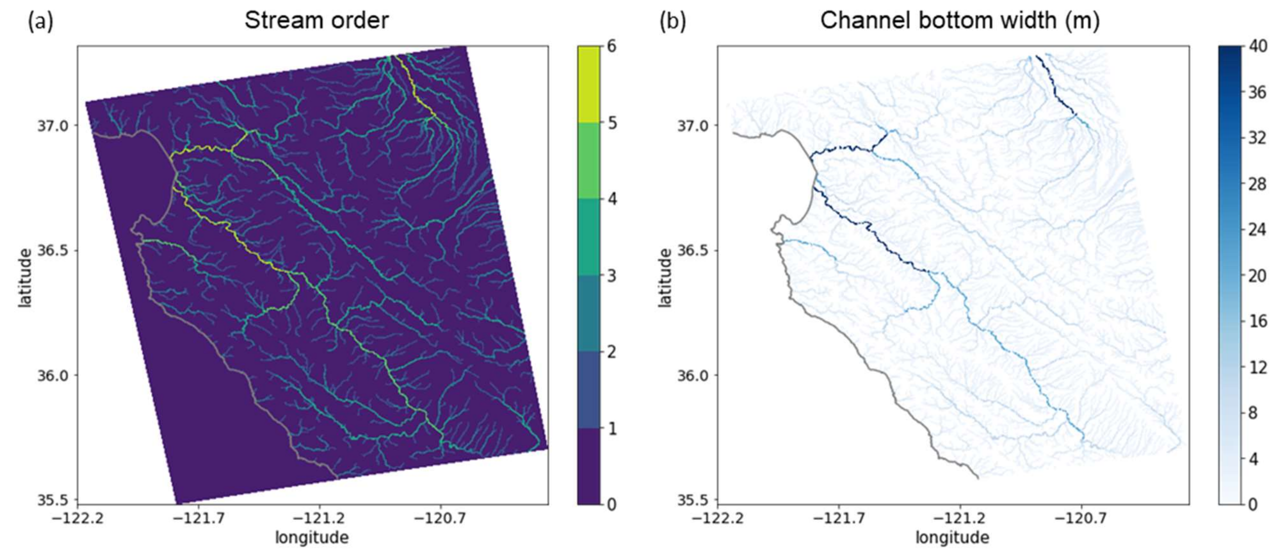

Fig. B3 (a) Stream order defined by the USGS 30-m DEM in our WRF-Hydro model domain and (b) the channel bottom width (m) which is a function of stream order (Table B1).

Table B2

MODIS IGBP 20-category land cover type and properties in Noah-MP LSM

Land cover code	Land cover type	Canopy height (m)	Max carboxylation rate at 25°C ($\mu mol\ CO_2/(m^2 \cdot s)$)	Overland flow roughness
1	Evergreen Needleleaf Forest	20	50	0.2
2	Evergreen Broadleaf Forest	20	60	0.2
3	Deciduous Needleleaf Forest	18	60	0.2
4	Deciduous Broadleaf Forest	16	60	0.2
5	Mixed Forests	16	55	0.2
6	Closed Shrublands	1.1	40	0.055
7	Open Shrublands	1.1	40	0.055
8	Woody Savannas	13	40	0.055
9	Savannas	10	40	0.055
10	Grasslands	1	40	0.055
11	Permanent wetlands	5	50	0.07
12	Croplands	2	80	0.035
13	Urban and Built-Up	15	0	0.025
14	Cropland/natural vegetation mosaic	1.5	60	0.035
15	Snow and Ice	0	0	0.01
16	Barren or Sparsely Vegetated	0	0	0.035
17	Water	0	0	0.005
18	Wooded Tundra	4	50	0.055
19	Mixed Tundra	2	50	0.055
20	Barren Tundra	0.5	50	0.055

Table B2 MODIS IGBP 20-category land cover type and properties in Noah-MP LSM.

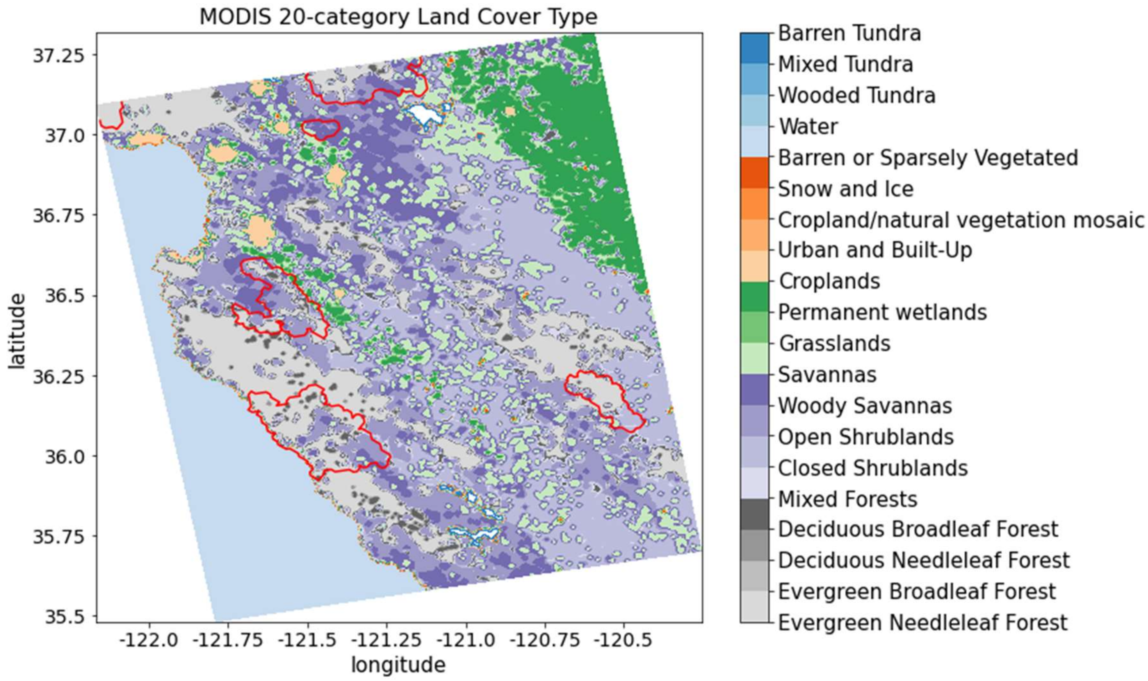

Fig. B4 MODIS IGBP 20-category land cover type in the model domain. Red polylines are 2020 wildfire burn scar perimeters.

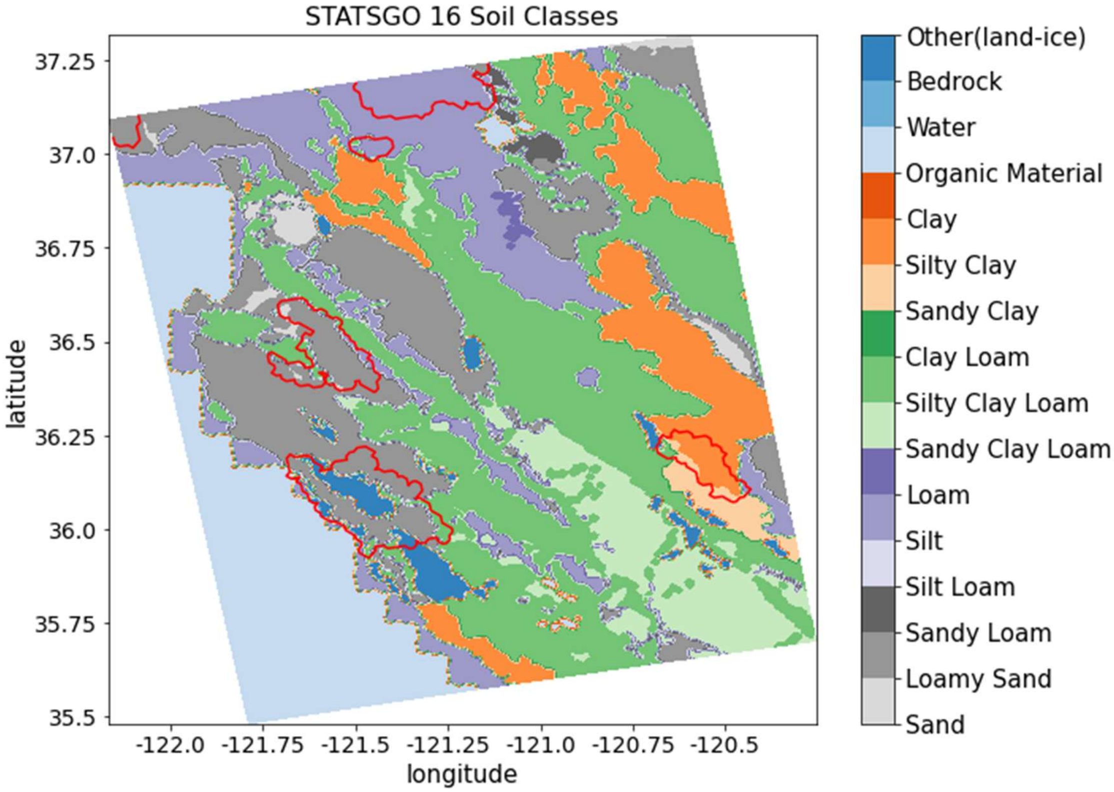

Fig. B5 1-km STATSGO data with 16 soil texture types. Red polylines are 2020 wildfire burn scar perimeters.

Table B3

Default and calibrated soil parameters in WRF-Hydro

Soil type	Default			After calibration		
	Grain size distribution index	Porosity	Saturated hydraulic conductivity ($m\ s^{-1}$)	Grain size distribution index	Porosity	Saturated hydraulic conductivity ($m\ s^{-1}$)
Sand	2.79	0.339	4.66E-5	2.51	0.315	$1.5 \times 10^{-7}\ m\ s^{-1}$ for all the burn scars, and original values elsewhere.
Loamy sand	4.26	0.421	1.41E-5	3.83	0.392	
Sandy loam	4.74	0.434	5.23E-6	4.27	0.404	
Silt loam	5.33	0.476	2.81E-6	4.80	0.442	
Silt	3.86	0.484	2.18E-6	3.47	0.450	
Loam	5.25	0.439	3.38E-6	4.73	0.408	
Sandy clay loam	6.77	0.404	4.45E-6	6.09	0.376	
Silty clay loam	8.72	0.464	2.03E-6	7.85	0.432	
Clay loam	8.17	0.465	2.45E-6	7.35	0.432	
Sandy clay	10.73	0.406	7.22E-6	9.66	0.378	
Silty clay	10.39	0.468	1.34E-6	9.35	0.435	
Clay	11.55	0.468	9.74E-7	10.40	0.435	
Organic material	5.25	0.439	3.38E-6	4.73	0.408	
Water	0.00	1.00	0.00	0.00	1.00	
Bedrock	2.79	0.200	1.41E-4	2.51	0.186	
Other	4.26	0.421	1.41E-5	3.83	0.392	
Playa	11.55	0.468	9.74E-7	10.40	0.435	
Lava	2.79	0.200	1.41E-4	2.51	0.186	
White sand	2.79	0.339	4.66E-5	2.51	0.315	

Table B3 Soil parameters in default and calibrated WRF-Hydro. Default soil parameters in WRF-Hydro are adapted from the soil analysis by Cosby et al. (1984). Grain size distribution index and soil porosity are altered from default values during the global soil moisture calibration. Saturated hydraulic conductivity is altered from default values during the streamflow calibration.

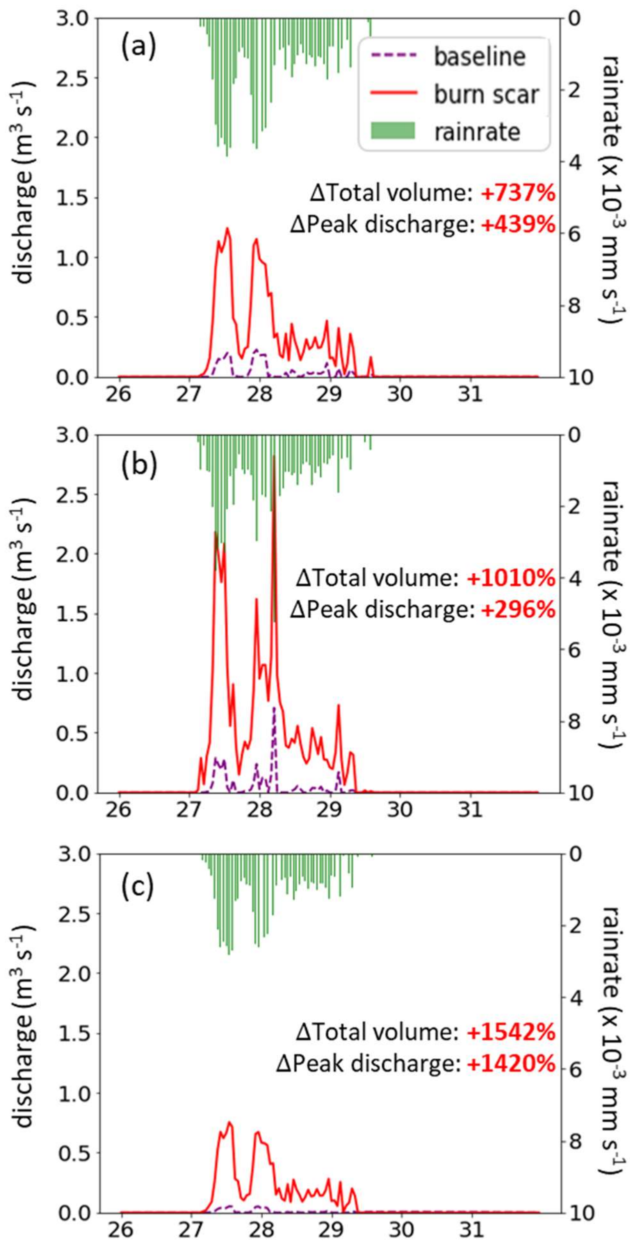

Fig. B6 WRF-Hydro simulated discharge time-series at four debris flow source areas. (a)–(c) MRMS precipitation (green bars) and simulated discharge time-series for January 26th 00:00 to 31st 23:00 at Mill Creek, Big Creek, and Nacimiento debris flow source areas (black circles in Fig. 7b–d) in baseline (purple dashed line) and burn scar simulation (red line).

Table B4

The total runoff volume, peak discharge, and peak timing at debris-flow source areas

Site name	Baseline simulation			Burn scar simulation		
	Total volume (m^3)	**Peak discharge (m^3 s^{-1})**	**Peak timing**	**Total volume (m^3)**	**Peak discharge (m^3 s^{-1})**	**Peak timing**
Mill Creek	10,023	0.23	27th 23:00	83,853 (+737%)	1.24 (+439%)	27th 13:00
Big Creek	11,611	0.71	28th 05:00	128,879 (+1010%)	2.81 (+296%)	28th 05:00
Nacimiento	3,031	0.05	27th 13:00	49,792 (+1542%)	0.76 (+1420%)	27th 13:00

Table B4 The total runoff volume, peak discharge, and peak timing in the baseline and burn scar simulations from January 27th 00:00 to 31st 23:00 at source areas of Rat Creek, Mill Creek, Big Creek, and Nacimiento debris flows (black circles in Fig. 7b–d). The percent change of the total volume and peak discharge in the burn scar simulation relative to the baseline simulation are shown in parentheses.

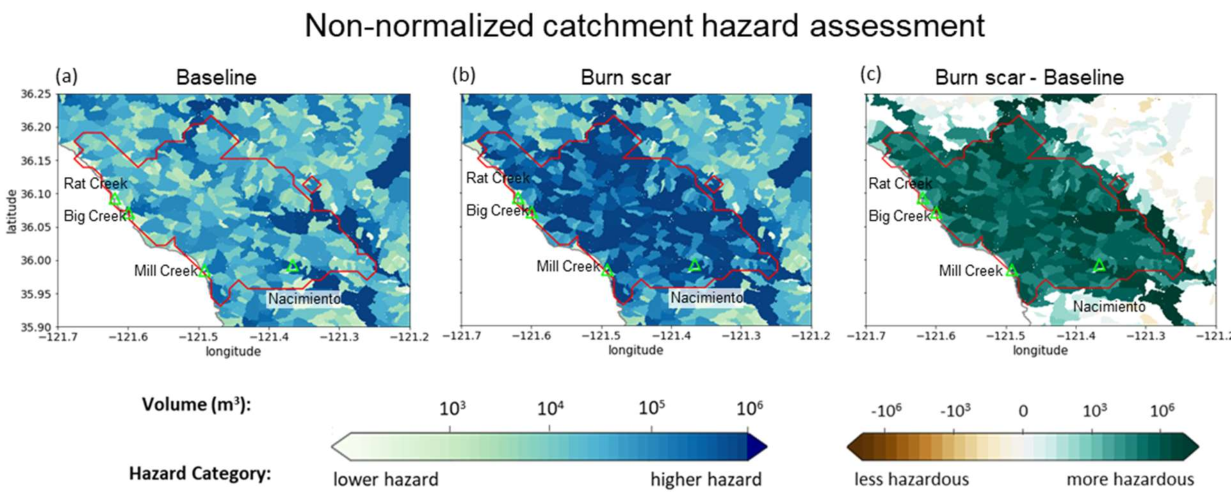

Fig. B7 Discharge volume-based runoff-generated debris flow hazard at catchment level in the (a) baseline simulation, (b) burn scar simulation, and (c) the difference between the burn scar and baseline simulations. For each catchment, the hazard is assessed by computing the total discharge volume at the catchment outlet from January 27th 00:00 to 28th 12:00.

Data availability statement

The NLDAS-2 reanalysis forcing data is publicly available at NASA GES DISC: https://disc.gsfc.nasa.gov/datasets?keywords=NLDAS. A detailed description can be found at https://ldas.gsfc.nasa.gov/nldas/v2/forcing. The MRMS radar-only precipitation estimate is publicly available at: https://mtarchive.geol.iastate.edu/. A description can be found at https://www.nssl.noaa.gov/projects/mrms/. The PSL in-situ soil moisture data is publicly available at: https://psl.noaa.gov/data/obs/datadisplay/. The USGS streamflow is publicly available at: https://waterdata.usgs.gov/nwis/. The remote sensing data used in this manuscript were provided by the European Space Agency (ESA) Copernicus program and accessed on Google Earth Engine (https://code.earthengine.google.com). All processed data required to reproduce the results of this study are archived on Zenodo at http://doi.org/10.5281/zenodo.5544083.

Code availability statement

The modified WRF-Hydro Fortran code and instructions to output the overland flow at terrain routing grid can be downloaded at https://github.com/NU-CCRG/Modified-WRF-Hydro.

HazMapper v1.0 is available at https://hazmapper.org/. The SAR backscatter change method code is available at https://github.com/MongHanHuang/GEE_SAR_landslide_detection.

Author contribution

Conceptualization: CL, ALH, & DEH; Simulation and model analysis: CL; JW & WY model methodological development. Remote sensing analysis: ALH; Field Observations: NJF; GIS assistance: YX; Funding acquisition: GB & DH; CL wrote the original draft and all authors reviewed and edited the manuscript.

Competing interests

The authors declare that they have no conflict of interest.

Acknowledgments

C.L., A.L.H., J.W., X.L., G.B., and D.E.H. acknowledge support from NSF PREEVENTS #1848683. We acknowledge high-performance computing support from Cheyenne (doi:10.5065/D6RX99HX) provided by NCAR's Computational and Information Systems Laboratory, sponsored by the National Science Foundation.

References

Anderson, H. W., Hoover, M. D., & Reinhart, K. G. (1976). Forests and water: effects of forest management on floods, sedimentation, and water supply (Vol. 18): Department of Agriculture, Forest Service, Pacific Southwest Forest and Range Experiment Station, Berkeley, CA.

Andersson, J. C. M., Arheimer, B., Traoré, F., Gustafsson, D., & Ali, A. (2017). Process refinements improve a hydrological model concept applied to the Niger River basin. Hydrological Processes, 31(25), 4540-4554. doi:https://doi.org/10.1002/hyp.11376

Arattano, M., & Franzi, L. (2010). On the application of kinematic models to simulate the diffusive processes of debris flows. Nat. Hazards Earth Syst. Sci., 10(8), 1689-1695. doi:10.5194/nhess-10-1689-2010

Arattano, M., & Savage, W. Z. J. B. o. t. I. A. o. E. G.-B. d. l. A. I. d. G. d. l. I. (1994). Modelling debris flows as kinematic waves. 49, 3-13.

Banihabib, M. E., Jurik, L., Kazemi, M. S., Soltani, J., & Tanhapour, M. (2020). A Hybrid Intelligence Model for the Prediction of the Peak Flow of Debris Floods. Water, 12(8). doi:10.3390/w12082246

Bart, R. (2016). A regional estimate of postfire streamflow change in California. Water Resources Research, 52, n/a-n/a. doi:10.1002/2014WR016553

Bart, R., & Hope, A. (2010). Streamflow response to fire in large catchments of a Mediterranean-climate region using paired-catchment experiments. Journal of Hydrology, 388, 370-378. doi:10.1016/j.jhydrol.2010.05.016

Bisson M, Favalli M, Fornaciai A, Mazzarini F, Isola I, Zanchetta G, Pareschi MT (2005) A rapid method to assess fire-related debris flow hazard in the Mediterranean region: An example from Sicily (southern Italy) International Journal of Applied Earth Observation and Geoinformation 7:217-231 doi:https://doi.org/10.1016/j.jag.2005.04.003

Bitew, M. M., & Gebremichael, M. (2011). Assessment of satellite rainfall products for streamflow simulation in medium watersheds of the Ethiopian highlands. Hydrol. Earth Syst. Sci., 15(4), 1147-1155. doi:10.5194/hess-15-1147-2011

Brown, E.K., Wang, J., & Feng, Y. (2020). U.S. wildfire potential: a historical view and future projection using high-resolution climate data. Environmental Research Letters. 16, 034060

Bytheway, J. L., Hughes, M., Mahoney, K., & Cifelli, R. (2020). On the Uncertainty of High-Resolution Hourly Quantitative Precipitation Estimates in California, Journal of Hydrometeorology, 21(5), 865-879. Retrieved Oct 25, 2021, from https://journals.ametsoc.org/view/journals/hydr/21/5/jhm-d-19-0160.1.xml

Camera, C., Bruggeman, A., Zittis, G., Sofokleous, I., & Arnault, J. (2020). Simulation of extreme rainfall and streamflow events in small Mediterranean watersheds with a one-way-coupled atmospheric-hydrologic modelling system. Natural hazards and earth system sciences, 20(10), 2791-2810. doi:10.5194/nhess-20-2791-2020

Canfield, H., Goodrich, D., & Burns, I. S. (2005). Selection of Parameters Values to Model Postfire Runoff and Sediment Transport at the Watershed Scale in Southwestern Forests.

Cannon, S., Gartner, J., C, P., & Parise, M. (2003). Widlfire-related debris flow generation through episodic progressive sediment-bulking processes, western USA (Vol. 1).

Cannon, S., Gartner, J., Wilson, R., Bowers, J., & Laber, J. (2008). Storm Rainfall Conditions for Floods and Debris Flows from Recently Burned Basins in Southwestern Colorado and Southern California. Geomorphology, 96, 250-269. doi:10.1016/j.geomorph.2007.03.019

Cannon, S. H. (2001). Debris flow generation from recently burned watersheds. Environmental & Engineering Geoscience, 7(4), 321-341.

Cannon, S. H., Boldt, E. M., Laber, J. L., Kean, J. W., & Staley, D. M. J. N. H. (2011). Rainfall intensity–duration thresholds for postfire debris flow emergency-response planning. 59(1), 209-236.

Cannon, S. H., & DeGraff, J. (2009). The increasing wildfire and postfire debris flow threat in western USA, and implications for consequences of climate change. In Landslides–disaster risk reduction (pp. 177-190): Springer.

Cannon, S. H., Gartner, J. E., Rupert, M. G., Michael, J. A., Rea, A. H., & Parrett, C. (2010). Predicting the probability and volume of postwildfire debris flows in the intermountain western United States. GSA Bulletin, 122(1-2), 127-144. doi:10.1130/B26459.1

Cerdà, A. (1998). Changes in overland flow and infiltration after a rangeland fire in a Mediterranean scrubland. Hydrological Processes, 12(7), 1031-1042. doi:https://doi.org/10.1002/(SICI)1099-1085(19980615)12:7<1031::AID-HYP636>3.0.CO;2-V

Chen, F., & Dudhia, J. (2001). Coupling an Advanced Land Surface–Hydrology Model with the Penn State–NCAR MM5 Modeling System. Part I: Model Implementation and Sensitivity, Monthly Weather Review, 129(4), 569-585. Retrieved Oct 24, 2021, from https://journals.ametsoc.org/view/journals/mwre/129/4/1520-0493_2001_129_0569_caalsh_2.0.co_2.xml

Chen, L., Berli, M., & Chief, K. (2013). Examining Modeling Approaches for the Rainfall-Runoff Process in Wildfire-Affected Watersheds: Using San Dimas Experimental Forest. JAWRA Journal of the American Water Resources Association, 49(4), 851-866. doi:https://doi.org/10.1111/jawr.12043

Reynolds, C., (2021, February 25). Highway 1 washout near Big Sur expected to be fixed by summer, Los Angeles Times. https://www.latimes.com/travel/story/2021-02-25/highway-1-to-big-sur-will-reopen-by-summer-caltrans-says

Coe, J., Godt, J., Parise, M., & Moscariello, A. (2003). Estimating debris flow probability using fan stratigraphy, historic records, and drainage-basin morphology, Interstate 70 highway corridor, central Colorado, USA. Paper presented at the Debris flow Hazards Mitigation: Mechanics, Prediction, and Assessment, edited by: Rickenmann, D. and Cheng, Ch., Proceedings 3rd International DFHM Conference, Davos, Switzerland.

Coe, J. A., Kinner, D. A., & Godt, J. W. J. G. (2008). Initiation conditions for debris flows generated by runoff at Chalk Cliffs, central Colorado. 96(3-4), 270-297.

Cosby, B. J., Hornberger, G. M., Clapp, R. B., & Ginn, T. R. (1984). A Statistical Exploration of the Relationships of Soil Moisture Characteristics to the Physical Properties of Soils. Water Resources Research, 20(6), 682-690. doi:https://doi.org/10.1029/WR020i006p00682

Cydzik, K., & Hogue, T. S. J. J. J. o. t. A. W. R. A. (2009). Modeling postfire response and recovery using the hydrologic engineering center hydrologic modeling system (HEC-HMS) 1. 45(3), 702-714.

Daly, C., R. P. Neilson, & D. L. Phillips. (1994). A statistical-topographic model for mapping climatological precipitation over mountainous terrain. J. Appl. Meteor., 33, 140–158, https://doi.org/10.1175/1520-0450(1994)033<0140:ASTMFM>2.0.CO;2.

Daly, C., M. E. Slater, J. A. Roberti, S. H. Laseter, & L. W. Swift Jr.. (2017). High-resolution precipitation mapping in a mountainous watershed; Ground truth for evaluating uncertainty in a national precipitation dataset. Int. J. Climatol., 37, 124–137, https://doi.org/10.1002/joc.4986.

Davies, T., Phillips, C., Pearce, A., & Zhang, X. J. I. P. (1992). Debris flow behaviour–an integrated overview. 209(21), 225.

Dekker, L. W., & Ritsema, C. J. (1994). How water moves in a water repellent sandy soil: 1. Potential and actual water repellency. Water Resources Research, 30(9), 2507-2517. doi:https://doi.org/10.1029/94WR00749

Di Cristo, C., Iervolino, M., Moramarco, T., & Vacca, A. (2021). Applicability of Diffusive model for mud-flows: An unsteady analysis. Journal of Hydrology, 600, 126512. doi:https://doi.org/10.1016/j.jhydrol.2021.126512

Doerr, S. H., & Thomas, A. (2000). The role of soil moisture in controlling water repellency: New evidence from forest soils in Portugal. Journal of Hydrology, 231-232, 134-147. doi:10.1016/S0022-1694(00)00190-6

Friedel, M.J. (2011a) A data-driven approach for modeling post-fire debris-flow volumes and their uncertainty Environmental Modelling & Software 26:1583-1598 doi:https://doi.org/10.1016/j.envsoft.2011.07.014

Friedel, M.J. (2011b) Modeling hydrologic and geomorphic hazards across post-fire landscapes using a self-organizing map approach Environmental Modelling & Software 26:1660-1674 doi:https://doi.org/10.1016/j.envsoft.2011.07.001

Gartner, J. E., Cannon, S. H., & Santi, P. M. (2014). Empirical models for predicting volumes of sediment deposited by debris flows and sediment-laden floods in the transverse ranges of southern California. Engineering Geology, 176, 45-56. doi:https://doi.org/10.1016/j.enggeo.2014.04.008

George, D. L., & Iverson, R. M. (2014). A depth-averaged debris flow model that includes the effects of evolving dilatancy. II. Numerical predictions and experimental tests. Proceedings of the Royal Society A: Mathematical, Physical and Engineering Sciences, 470(2170), 20130820. doi:10.1098/rspa.2013.0820

Gochis, D. J., & Chen, F. (2003). Hydrological Enhancements to the Community Noah Land Surface Model (No. NCAR/TN-454+STR). University Corporation for Atmospheric Research. doi:10.5065/D60P0X00

Goodrich, D., Burns, I., Unkrich, C., Semmens, D., Guertin, D., Hernandez, M., . . . Levick, L. (2012). KINEROS2/AGWA: model use, calibration, and validation. Transactions of the ASABE, 55, 1561-1574. doi:10.13031/2013.42264

Goss, M., Swain, D. L., Abatzoglou, J. T., Sarhadi, A., Kolden, C. A., Williams, A. P., & Diffenbaugh, N. S. (2020). Climate change is increasing the likelihood of extreme autumn wildfire conditions across California. Environmental Research Letters, 15(9), 094016. doi:10.1088/1748-9326/ab83a7

Gregoretti, C., & Fontana, G. D. (2008). The triggering of debris flow due to channel-bed failure in some alpine headwater basins of the Dolomites: analyses of critical runoff. Hydrological Processes, 22(13), 2248-2263. doi:https://doi.org/10.1002/hyp.6821

Gupta, H. V., Kling, H., Yilmaz, K. K., & Martinez, G. F. (2009). Decomposition of the mean squared error and NSE performance criteria: Implications for improving hydrological modelling. Journal of Hydrology, 377(1), 80-91. doi:https://doi.org/10.1016/j.jhydrol.2009.08.003

Handwerger, A. L., Jones, S. Y., Amatya, P., Kerner, H. R., Kirschbaum, D. B., and Huang, M.-H. (in review): Strategies for landslide detection using open-access synthetic aperture radar backscatter change in Google Earth Engine, Nat. Hazards Earth Syst. Sci. Discuss.

Huang, X., Swain, D. L., & Hall, A. D. (2020). Future precipitation increase from very high resolution ensemble downscaling of extreme atmospheric river storms in California. 6(29), eaba1323. doi:10.1126/sciadv.aba1323 %J Science Advances

Ice, G. G., Neary, D. G., & Adams, P. W. (2004). Effects of Wildfire on Soils and Watershed Processes. Journal of Forestry, 102(6), 16-20. doi:10.1093/jof/102.6.16

Iverson, R. M., & George, D. L. (2014). A depth-averaged debris flow model that includes the effects of evolving dilatancy. I. Physical basis. Proceedings of the Royal Society A: Mathematical, Physical and Engineering Sciences, 470(2170), 20130819. doi:10.1098/rspa.2013.0819

Jolly, W. M., Cochrane, M. A., Freeborn, P. H., Holden, Z. A., Brown, T. J., Williamson, G. J., & Bowman, D. M. J. S. (2015). Climate-induced variations in global wildfire danger from 1979 to 2013. Nature Communications, 6(1), 7537. doi:10.1038/ncomms8537

Julien, P. Y., Saghafian, B., & Ogden, F. L. (1995). RASTER-BASED HYDROLOGIC MODELING OF SPATIALLY-VARIED SURFACE RUNOFF1. JAWRA Journal of the American Water Resources Association, 31(3), 523-536. doi:https://doi.org/10.1111/j.1752-1688.1995.tb04039.x

Kean, J. W., McCoy, S. W., Tucker, G. E., Staley, D. M., & Coe, J. A. (2013). Runoff-generated debris flows: Observations and modeling of surge initiation, magnitude, and frequency. Journal of Geophysical Research: Earth Surface, 118(4), 2190-2207. doi:https://doi.org/10.1002/jgrf.20148

Kean, J. W., & Staley, D. M. (2021). Forecasting the Frequency and Magnitude of Postfire Debris Flows Across Southern California. Earth's Future, 9(3), e2020EF001735. doi:https://doi.org/10.1029/2020EF001735

Kean, J. W., Staley, D. M., & Cannon, S. H. (2011). In situ measurements of postfire debris flows in southern California: Comparisons of the timing and magnitude of 24 debris flow events with rainfall and soil moisture conditions. Journal of Geophysical Research F: Earth Surface, 116(4). doi:10.1029/2011JF002005

Kinoshita, A. M., & Hogue, T. S. (2015). Increased dry season water yield in burned watersheds in Southern California. Environmental Research Letters, 10(1), 014003. doi:10.1088/1748-9326/10/1/014003

Kling, H., Fuchs, M., & Paulin, M. (2012). Runoff conditions in the upper Danube basin under an ensemble of climate change scenarios. Journal of Hydrology, 424-425, 264-277. doi:https://doi.org/10.1016/j.jhydrol.2012.01.011

Larsen, I., MacDonald, L., Brown, E., Rough, D., Welsh, M., Pietraszek, J., . . . Schaffrath, K. (2009). Causes of Postfire Runoff and Erosion: Water Repellency, Cover, or Soil Sealing? Soil Science Society of America Journal - SSSAJ, 73. doi:10.2136/sssaj2007.0432

Lahmers, T. M., Gupta, H., Castro, C. L., Gochis, D. J., Yates, D., Dugger, A., . . . Hazenberg, P. J. J. o. H. (2019). Enhancing the structure of the WRF-Hydro hydrologic model for semiarid environments. 20(4), 691-714.

Lahmers, T. M., Castro, C. L., & Hazenberg, P. (2020). Effects of Lateral Flow on the Convective Environment in a Coupled Hydrometeorological Modeling System in a Semiarid Environment, Journal of Hydrometeorology, 21(4), 615-642. Retrieved Sep 29, 2021, from https://journals.ametsoc.org/view/journals/hydr/21/4/jhm-d-19-0100.1.xml

MacDonald, L. H., & Huffman, E. L. (2004). Postfire soil water repellency: Persistence and soil moisture thresholds. Soil Science Society of America Journal, 68, 1729-1734.

Martin, D., & Moody, J. (2001). Comparison of Soil Infiltration Rates in Burned and Unburned Mountainous Watersheds. Hydrological Processes, 15, 2893-2903. doi:10.1002/hyp.380

McGuire, L. A., Rengers, F. K., Kean, J. W., & Staley, D. M. (2017). Debris flow initiation by runoff in a recently burned basin: Is grain-by-grain sediment bulking or en masse failure to blame? Geophysical Research Letters, 44(14), 7310-7319. doi:https://doi.org/10.1002/2017GL074243

McGuire, L. A., & Youberg, A. M. (2020). What drives spatial variability in rainfall intensity-duration thresholds for post-wildfire debris flows? Insights from the 2018 Buzzard Fire, NM, USA. Landslides, 17(10), 2385-2399. doi:10.1007/s10346-020-01470-y

McMichael, C. E., & Hope, A. S. (2007). Predicting streamflow response to fire-induced landcover change: implications of parameter uncertainty in the MIKE SHE model. J Environ Manage, 84(3), 245-256. doi:10.1016/j.jenvman.2006.06.003

Meixner, T., & Wohlgemuth, P. (2003). Climate Variability, Fire, Vegetation Recovery, and Watershed Hydrology.

Meyer, G. A., & Wells, S. G. (1997). Fire-related sedimentation events on alluvial fans, Yellowstone National Park, U.S.A. Journal of Sedimentary Research, 67(5), 776-791. doi:10.1306/D426863A-2B26-11D7-8648000102C1865D

Mikoš, M., & Bezak, N. (2021). Debris Flow Modelling Using RAMMS Model in the Alpine Environment With Focus on the Model Parameters and Main Characteristics. 8(732). doi:10.3389/feart.2020.605061

Miller, D. A., & White, R. A. (1998). A Conterminous United States Multilayer Soil Characteristics Dataset for Regional Climate and Hydrology Modeling, Earth Interactions, 2(2), 1-26. Retrieved Sep 27, 2021, from https://journals.ametsoc.org/view/journals/eint/2/2/1087-3562_1998_002_0001_acusms_2.3.co_2.xml

Mitsopoulos, I. D., & Mironidis, D. (2006). Assessment of post fire debris flow potential in a Mediterranean type ecosystem. WIT Transactions on Ecology and the Environment, 90.

Moody, J., & Ebel, B. (2012). Hyper-dry conditions provide new insights into the cause of extreme floods after wildfire. CATENA, 93, 58-63. doi:10.1016/j.catena.2012.01.006

Moody, J., Shakesby, R., Robichaud, P., Cannon, S., & Martin, D. A. J. E.-S. R. (2013). Current research issues related to post-wildfire runoff and erosion processes. 122, 10-37.

Moriasi, D. N., Arnold, J. G., Van Liew, M. W., Bingner, R. L., Harmel, R. D., & Veith, T. L. (2007). Model evaluation guidelines for systematic quantification of accuracy in watershed simulations. Transactions of the ASABE, 50(3), 885-900.

Nash, J. E., & Sutcliffe, J. V. (1970). River flow forecasting through conceptual models part I — A discussion of principles. Journal of Hydrology, 10(3), 282-290. doi:https://doi.org/10.1016/0022-1694(70)90255-6

Neary, D., Gottfried, G., & Ffolliott, P. (2003). Post-wildfire watershed flood responses.

Nikolopoulos, E.I., Destro, E., Bhuiyan, M.A.E, Borga, M., & Anagnostou, E.N. (2018). Evaluation of predictive models for postfire debris flow occurrence in the western United States Nat Hazards Earth Syst Sci 18:2331-2343 doi:10.5194/nhess-18-2331-2018

Niu G-Y et al. (2011) The community Noah land surface model with multiparameterization options (Noah-MP): 1. Model description and evaluation with local-scale measurements J Geophys Res Atm 116 doi:https://doi.org/10.1029/2010JD015139

Nyman, P., Smith, H. G., Sherwin, C. B., Langhans, C., Lane, P. N. J., & Sheridan, G. J. (2015). Predicting sediment delivery from debris flows after wildfire. Geomorphology, 250, 173-186. doi:https://doi.org/10.1016/j.geomorph.2015.08.023

Oakley, N. S. (2021). A warming climate adds complexity to postfire hydrologic hazard planning. Earth's Future, 9, e2021EF002149. https://doi.org/10.1029/2021EF002149

Ogden, F. L. J. D. o. C., & Environmental Engineering, U. o. C., Storrs. (1997). CASC2D reference manual.

Parise, M, Cannon, S.H. (2008) The effects of wildfires on erosion and debris-flow generation in Mediterranean climatic areas: a first database. Proceedings of 1st World Landslide Forum. Tokyo, Japan, pp 465–468

Parise, M., & Cannon, S. H. (2009, April). A database on post-fire erosion rates and debris flows in Mediterranean-Basin watersheds. In EGU General Assembly Conference Abstracts (p. 1530).

Parise, M., Cannon, S.H. (2012) Wildfire impacts on the processes that generate debris flows in burned watersheds Nat Hazards 61:217-227 doi:10.1007/s11069-011-9769-9

Polade, S.D., Gershunov, A., Cayan, D.R, Dettinger, MD, & Pierce, D.W. (2017) Precipitation in a warming world: Assessing projected hydro-climate changes in California and other Mediterranean climate regions Scientific Reports 7:10783 doi:10.1038/s41598-017-11285-y

Qi, Y., S. Martinaitis, J. Zhang, & S. Cocks. (2016). A real-time automated quality control of hourly rain gauge data based on multiple sensors in MRMS system. J. Hydrometeor., 17, 1675–1691, https://doi.org/10.1175/JHM-D-15-0188.1.

Rengers, F. K., McGuire, L. A., Kean, J. W., Staley, D. M., & Hobley, D. E. J. (2016). Model simulations of flood and debris flow timing in steep catchments after wildfire. Water Resources Research, 52(8), 6041-6061. doi:https://doi.org/10.1002/2015WR018176

Robichaud, P., Beyers, J., & Neary, D. (2000). Evaluating the effectiveness of postfire rehabilitation treatments.

Rosso R, Rulli MC, Bocchiola D (2007) Transient catchment hydrology after wildfires in a Mediterranean basin: runoff, sediment and woody debris Hydrol Earth Syst Sci 11:125-140 doi:10.5194/hess-11-125-2007

Rulli, M. C., & Rosso, R. (2007). Hydrologic response of upland catchments to wildfires. Advances in Water Resources, 30(10), 2072-2086. doi:https://doi.org/10.1016/j.advwatres.2006.10.012

Santi, P. M., deWolfe, V. G., Higgins, J. D., Cannon, S. H., & Gartner, J. E. (2008). Sources of debris flow material in burned areas. Geomorphology, 96(3-4), 310-321. doi:10.1016/j.geomorph.2007.02.022

Santi, P. M., & Morandi, L. (2013). Comparison of debris flow volumes from burned and unburned areas. Landslides, 10(6), 757-769.

Schaefli, B., & Gupta, H. V. (2007). Do Nash values have value? Hydrological Processes, 21(15), 2075-2080. https://doi.org/10.1002/hyp.6825

Scheip, C. M., & Wegmann, K. W. (2021). HazMapper: A global open-source natural hazard mapping application in Google Earth Engine. Natural Hazards and Earth System Sciences, 21(5), 1495-1511.

Schönfelder, L., Bakken, T., Alfredsen, K., & Adera, A. (2017). Application of HYPE in Norway.

Scott, D. F., & Van Wyk, D. B. (1990). The effects of wildfire on soil wettability and hydrological behaviour of an afforested catchment. 121, 239. doi:10.1016/0022-1694(90)90234-o

Scott, D. J. J. o. H. (1993). The hydrological effects of fire in South African mountain catchments. 150, 409-432.

Shakesby, R. A., & Doerr, S. H. (2006). Wildfire as a hydrological and geomorphological agent. Earth-Science Reviews, 74(3), 269-307. doi:https://doi.org/10.1016/j.earscirev.2005.10.006

Shen H, Lynch, B., Poulsen, C.J., & Yanites, B.J. (2021) A modeling framework (WRF-Landlab) for simulating orogen-scale climate-erosion coupling Computers & Geosciences 146:104625 doi:https://doi.org/10.1016/j.cageo.2020.104625

Sidman, G., Guertin, D., Goodrich, D., Unkrich, C., & Burns, I. (2016). Risk assessment of post-wildfire hydrological response in semiarid basins: the effects of varying rainfall representations in the KINEROS2/AGWA model. International Journal of Wildland Fire, 25, 268-278. doi:10.1071/WF14071

Staley, D. M., Negri, J. A., Kean, J. W., Laber, J. L., Tillery, A. C., & Youberg, A. M. (2016). Updated logistic regression equations for the calculation of postfire debris flow likelihood in the western United States (2016-1106). Retrieved from Reston, VA: http://pubs.er.usgs.gov/publication/ofr20161106

Stoof, C. R., Vervoort, R. W., Iwema, J., van den Elsen, E., Ferreira, A. J. D., & Ritsema, C. J. (2012). Hydrological response of a small catchment burned by experimental fire. Hydrol. Earth Syst. Sci., 16(2), 267-285. doi:10.5194/hess-16-267-2012

Swain, D. L. (2021). A Shorter, Sharper Rainy Season Amplifies California Wildfire Risk. Geophysical Research Letters, 48(5), e2021GL092843. doi:https://doi.org/10.1029/2021GL092843

Swain, D. L., Langenbrunner, B., Neelin, J. D., & Hall, A. (2018) Increasing precipitation volatility in twenty-first-century California Nature Climate Change 8:427-433 doi:10.1038/s41558-018-0140-y

Tognacca, C., Bezzola, G., & Minor, H.-E. (2000). Threshold criterion for debris flow initiation due to channel-bed failure. Paper presented at the Debris flow hazards mitigation: Mechanics, prediction and assessment.

U.S. Forest Service, Burned Area Emergency Response, Dolan Postfire BAER Soil Burn Severity Map Released, October 10, 2020, https://inciweb.nwcg.gov/photos/CALPF/2020-10-06-1821-Dolan-PostFire-BAER/related_files/pict20200910-143346-0.pdf

U.S. Forest Service, Burned Area Emergency Response, Dolan Fire Burned Area Report, October 13, 2020, https://inciweb.nwcg.gov/photos/CALPF/2020-10-06-1821-Dolan-PostFire-BAER/related_files/pict20200927-132609-0.pdf

U.S. Geological Survey, Postfire Debris flow Hazards: Dolan Fire (Los Padres National Forest, CA), Landslide Hazards Program, retrieved September 27, 2021, from https://landslides.usgs.gov/hazards/postfire_debrisflow/detail.php?objectid=312

Vergopolan, N., Chaney, N. W., Beck, H. E., Pan, M., Sheffield, J., Chan, S., & Wood, E. F. (2020). Combining hyper-resolution land surface modeling with SMAP brightness temperatures to obtain 30-m soil moisture estimates. Remote Sensing of Environment, 242, 111740. doi:https://doi.org/10.1016/j.rse.2020.111740

Wang, J., Wang, C., Rao, V., Orr, A., Yan, E., & Kotamarthi, R. (2019). A parallel workflow implementation for PEST version 13.6 in high-performance computing for WRF-Hydro version 5.0: a case study over the midwestern United States. Geoscientific Model Development, 12(8), 3523-3539. doi:10.5194/gmd-12-3523-2019

Williams, A. P., Abatzoglou, J. T., Gershunov, A., Guzman-Morales, J., Bishop, D. A., Balch, J. K., & Lettenmaier, D. P. (2019). Observed Impacts of Anthropogenic Climate Change on Wildfire in California. Earth's Future, 7(8), 892-910. doi:https://doi.org/10.1029/2019EF001210

Xia, Y., Mitchell, K., Ek, M., Cosgrove, B., Sheffield, J., Luo, L., . . . Lohmann, D. (2012). Continental-scale water and energy flux analysis and validation for North American Land Data Assimilation System project phase 2 (NLDAS-2): 2. Validation of model-simulated streamflow. Journal of Geophysical Research: Atmospheres, 117(D3). doi:https://doi.org/10.1029/2011JD016051

Zhang, J. et al. (2011). National Mosaic and Multi-Sensor QPE (NMQ) system: Description, results, and future plans. Bull. Amer. Meteor. Soc., 92, 1321–1338, https://doi.org/10.1175/2011BAMS-D-11-00047.1.

Zhang, J., Y. Qi, C. Langston, B., Kaney, & K. Howard. (2014). A real-time algorithm for merging radar QPEs with rain gauge observations and orographic precipitation climatology. J. Hydrometeor., 15, 1794–1809, https://doi.org/10.1175/JHM-D-13-0163.1.

Zhang, J. et al. (2016). Multi-Radar Multi-Sensor (MRMS) quantitative precipitation estimation: Initial operating capabilities. Bull. Amer. Meteor. Soc., 97, 621–638, https://doi.org/10.1175/BAMS-D-14-00174.1.